

Aus der Klinik und Poliklinik für Radiologie
Klinik der Ludwig-Maximilians-Universität München
Direktor: Prof. Dr. med. Jens Ricke

Novel image processing methods for characterizing lung structure and function

Kumulative Dissertation
zum Erwerb des Doktorgrades der Humanbiologie
an der Medizinischen Fakultät der
Ludwig-Maximilians-Universität zu München

vorgelegt von
David Bondesson
aus Saxtorp
2020

Mit Genehmigung der Medizinischen Fakultät

Der Universität München

Berichterstatter: Prof. Dr. med. Julien Dinkel

Mitberichterstatter: Prof. Dr. Med. Rudolf Maria Huber

Prof. Dr. Thorsten Johnson

Priv. Doz. Dr. Tobias Heer

Dekan: Prof. Dr. med. dent. Reinhard Hickel

Tag der mündlichen Prüfung: 25.11.2020

Kumulative Dissertation

Contents

1.	Introduction	1
1.1	Lung diseases	2
1.1.1	DPLDs	2
1.1.2	PH.....	3
1.2	Probe Based Confocal Laser Endomicroscopy	4
1.2.1	Image Acquisition	4
1.2.2	Automated evaluation of Probe-based Confocal Laser Endomicroscopy in the lung – Own contribution.....	5
1.3	MRI	6
1.3.1	Magnetic Resonance Imaging	7
1.3.2	MRI of the Lungs	13
1.3.3	Non-uniform Fourier decomposition MRI for ventilation and perfusion weighted imaging of the lung – Own contribution	14
2.	Summary/Zusammenfassung	16
2.1	Automated evaluation of Probe-based Confocal Laser Endomicroscopy in the lung	16
2.2	Non-uniform Fourier decomposition MRI for ventilation and perfusion weighted imaging of the lung.....	18
3.	Original publications	20
3.1	Bondesson D, Schneider MJ, Silbernagel E, Behr J, Reichenberger F, Dinkel J (2020) Automated evaluation of probe-based confocal laser endomicroscopy in the lung. PLoS ONE 15(5): e0232847. https://doi.org/10.1371/journal.pone.0232847	20
3.2	Bondesson D, Gaass T, Dinkel J, Kiefer B. Non-contrast-enhanced perfusion and ventilation assessment of the human lung by means of wavelet decomposition in proton MRI. <i>Proc Intl Soc Mag Reson Med</i> 2016; 24:1934. https:// doi-org.emedien.ub.uni-muenchen.de/10.1002/mrm.27803 32	
4.	Additional Contributions	43
4.1	Silbernagel E, Bondesson D, Behr J, Dinkel J, Reichenberger F. Taking another view on lung fibrosis. <i>Am J Respir Crit Care Med</i> 2018;197:947–948. https://www.atsjournals.org/doi/10.1164/rccm.201708-1683IM	43
5.	List of abbreviations	47
6.	References	49
7.	Acknowledgements	62
8.	Affidavit	63

1. Introduction

The lungs are the most fundamental organs of the respiratory system. Their primary role is to facilitate gas exchange from the air into the blood. This is performed via two mechanisms that are working in conjunction: ventilation and perfusion. Ventilation is seen at the macroscopic level, where mechanically generated negative pressure within the lungs and pleural space allows air to be drawn in during the inhalation phase. consecutively, the decrease in lung volume during exhalation increases the pressure in the lungs, forcing the air out. The effect of perfusion on the other hand occurs at the microscopic level. It ensures that oxygen is transported through the alveoli into the capillary network, where it can enter the arterial system. A disorder or disease of the airway that affects these mechanics is defined as “respiratory disease” (1). Respiratory diseases impose a staggering burden on today’s society, impacting hundreds of millions and killing over 4 million people a year (2).

Imaging plays several important roles for the diagnostic workup to detect and identify specific respiratory diseases. It can be used for screening, differential diagnosis and monitoring of disease (3). In particular, radiological methods such as chest radiography (X-ray), computer tomography (CT) and magnetic resonance imaging (MRI) are used for pattern localization and assessment as well as evaluating regional distribution of involvement. Chest X-ray and CT are gold standard methods for morphological imaging, visualizing particular changes related to a subset of pulmonary pathologies (4). However, both (and especially CT) suffer from the downside of radiation exposure to the patient, which particularly for those with chronic illnesses will accumulate. Also, both are limited to only morphological evaluation, despite some novel methods in CT evaluating the lungs at their functional interface (5). MRI, in comparison, has a higher soft tissue contrast and does not expose the patient to ionizing radiation. This facilitates dynamic imaging ideal for functional evaluation and has been used to map the cardiopulmonary interactions as well as the impact of specific respiratory diseases on it (6). On the topic of functional lung evaluation with MRI, a method called Fourier decomposition (FD) has been presented, which is able to generate simultaneous ventilation and perfusion maps (7). These have been shown to display localized effects from several lung pathologies and potentially facilitate diagnosis (8–10). However, their evaluation assumes that the patients’ breathing and perfusion frequency remains constant between cycles throughout a 1-2 minute measurement. This would be a problem already for healthy people due to natural occurring ventilation- and heart rate-variability, but patients with respiratory problems can show especially strong variation. For some complex diagnostic situations such as with diffuse parenchymal lung disease (DPLD) it may be required to evaluate the micro architecture (i.e. alveoli structure) of the lungs (11). This is the case when clinical and radiological data is not sufficient for a diagnostic conclusion and lung biopsy/sampling might be required to complement the

data. The biopsies are performed through a bronchoscope which provides access and guidance through the bronchial tree to find appropriate sampling locations (12). Decisions to perform a biopsy are always weighed between the probability of increasing diagnostic and treatment certainty against risk of complications (13). These complications include pneumothorax, haemorrhage and exacerbation of the DPLD (14). Recently, a new bronchoscopy-guided imaging method called probe-based confocal laser endomicroscopy (pCLE) was introduced, promising a less invasive microscopic visualization of the lower respiratory tract (15). However, even with pCLE structural assessment is mostly performed visually by pulmonologists risking a high intra- and inter-reader variability.

This work has focused on developing two novel diagnostic methods. The first method concentrates on the macroscopic level, evaluating respiratory mechanics of ventilation and perfusion. This is a post processing algorithm that aims to address the effects of irregular breathing and cardiac frequency variation when applying FD on MR image sets. By accounting for frequency variability when generating ventilation and perfusion maps, a larger part of the respective signal variations could be utilized.

The second method aims to evaluate the microstructure of the lung using automated segmentation and quantification of essential structures in pCLE snapshots selected by pulmonologists during standard examination. As current structural workflow relies on measures such as human observation and manually selected measurements, assessment could become more objective with decreased variability.

1.1 Lung diseases

Lung diseases comprise of a wide array of illnesses. They are characterised based on where they are situated and if they are chronic or acute. Chronic respiratory diseases are further divided into obstructive or restrictive diseases (16). In the following section we will focus particularly on several DPLDs, as well as pulmonary hypertension (PH). DPLDs are part of chronic obstructive and restrictive lung diseases, whereas PH oftentimes follows as results of the two (17). Both pathologies will be introduced followed by the potential of pCLE for diagnosis of DPLDs and of MRI for the diagnosis of PH.

1.1.1 DPLDs

DPLDs constitutes more than 200 entities, heterogeneously affecting lung parenchyma or pulmonary interstitium. These include a multitude of pathologies with similar clinical, radiological and lung function characteristics (18). They are usually referred to as interstitial lung diseases (ILD), although ILDs also includes diseases affecting alveolar space. DPLDs have a low prevalence (26/100 000 for females and 32/100 000 for males) compared to other pulmonary pathologies (19), but oftentimes a much higher mortality rate and general effect on quality of life (20). They present with varying

prognoses and disease behaviour, complicating simple classification. Instead specific pathologies are characterized by degrees of inflammation, fibrosis and whether the cause is known or unknown(21).

Diagnosis of specific DPLDs is to this day a complex task since they share clinical, radiographic, physiological and pathological manifestations. High resolution CT (HRCT) is considered central amongst imaging modalities for detecting, and diagnosing many DPLDs (22) as it offers higher accuracy or lower adverse side effects compared to chest radiography and lung biopsy, respectively (23, 24). For these reasons, it has been specifically recommended for follow-up examinations to track efficacy of treatment, disease progression and complications (25–27). However, despite its advantages HRCT still struggles to yield consensus in the multi-disciplinary discussions. This is due to a large inter-rater variability, sometimes requiring further cytological and histological information (21, 28–30).

1.1.2 PH

Pulmonary hypertension (PH) is a disease associated with increased mortality and morbidity (31). Its total prevalence is unknown but estimates range between 5-52 cases per million people (32–36). It is characterized by a progressive increase of blood pressure within the arteries of the lungs leading to shortness of breath, syncope, tiredness, chest pain, swelling of the legs, and a fast heartbeat (37). Furthermore, if the mean pulmonary arterial pressure persists it could lead to irreversible remodelling of the pulmonary vasculature and eventually right heart failure (38, 39). PH is divided into five main subgroups categorizing these into pathophysiological mechanisms, clinical presentation, and therapeutic options (37):

1. pulmonary arterial hypertension (PAH)
2. PH due to left-heart disease
3. PH due to lung disease and hypoxia
4. chronic thromboembolic disease (CTEPH)
5. PH due to unclear and/or multifactorial mechanisms

Imaging modalities have a central role for detecting and classifying PH. For example, they facilitate tracking of treatment response, identification of potential underlying pathologies or non-invasive pulmonary pressure measurements (40). Amongst the standard diagnostic workup are echocardiography, CT and ventilation/perfusion (V/Q) scans, but a multitude of advanced imaging methods have presented new possibilities (41). Several of those are based on MRI, which has been highlighted for prognostic assessment and evaluation of CTEPH particularly (40). Standard diagnostic methods of CTEPH include either a V/Q scintigraphy scan or CT pulmonary angiography (CTPA) which can both exclude CTEPH with high sensitivity, specificity and accuracy (42). However, they both

expose patient to ionized radiation, which for long term patients will accumulate over many scans. Of the presented MRI methods, several aim to avoid contrast enhanced measurements (43–48), due to concerns of lasting depositions in brain skin and bones from the commonly used agent, gadolinium (49, 50).

1.2 Probe Based Confocal Laser Endomicroscopy

To address the issue of inter-rater variability of HRCT as well as the invasive procedure of biopsies in diagnosis of DPLDs, pCLE has been presented as a novel imaging technique. It provides real time imaging of the respiratory tract and alveolar ducts based on the microstructures' autofluorescence (51).

Having overcome initial technical limitations of low specificity, it now offers in vivo visualization (52–55). Having displayed structures correlating with histopathology in lung cancer, pCLE has raised the hope for a potential 'optical biopsy' as alternative to normal (56). Furthermore, Several studies have also showed its ability to track structural changes caused by different DPLDs (57–60). Specifically, increased elastin fibre thickness and density as well as number of cellular structures has been highlighted as important features that can be visualized with pCLE. However, previous DPLD studies with pCLE have relied on qualitative expert observer evaluation (57) or manual post processing methods (61, 62). If instead a process could automatically yield quantitative confirmation (aside from image selection), it would decrease diagnostic uncertainty for the examining pneumologists.

1.2.1 Image Acquisition

Since, the full alveoli image acquisition workflow has been previously described (63) only a shortened description will be given in the following section.

The procedure is performed by firstly inserting the confocal mini probe into the working channel of a flexible bronchoscope. Patients receive a topical anaesthesia of the airways and are put in supine position for insertion of the bronchoscope. The bronchoscope is pushed down to the smallest reachable bronchi and followed by the advancement of the mini probe. It is pushed inside the working channel through the distal bronchiole until it reaches the alveolar system. The 1.4 mm probe ensures a deeper reach in the bronchial structure compared to the bronchoscope. Its laser light with a wavelength of $488nm$ has been shown to mainly excite autofluorescence from the elastin content in the alveoli structures. The probe is manually applied onto bronchial surfaces of the trachea or the bronchus to produce images and considerations are taken not to damage sensitive tissue. Video shots are acquired at 9-12 images/second, penetrating between 0 to $50\ \mu m$ below the applied surface. Lateral and axial resolutions of the probe are $3.5\ \mu m$, and $15\ \mu m$, respectively. The images offer a field-of-view diameter as large as $600\ \mu m$, meaning that only a small part of the bronchial surface can be imaged simultaneously. However, since the probe

can be moved without much added risk multiple regions can be evaluated per examination. The average added duration of the pCLE procedure is 11 minutes and the current workflow has the shots stored for later analysis.

1.2.2 Automated evaluation of Probe-based Confocal Laser Endomicroscopy in the lung – Own contribution

To address the qualitative approach of previous evaluation workflows and show the potential of automatic evaluation during examination, a two-step approach was considered:

1. Develop a method for quantifying the alveoli elastin structures observed in the pCLE snapshots.
2. Present a prototype of a fully automated workflow to assess doctors' selected pCLE snapshots.

Structural connectivity and two statistical elements based on the localized thickness estimates (64), applied on a binarization (65) of the selected snapshots emerged after testing several methods. I evaluated the three values on one snapshot from healthy tissue and one from tissue struck by IPF in a case report (66). The case study is included as additional contribution (Section 4.1 bellow) to provide context for the follow up publication. In the report I showed heightened quantitative values for the IPF case with all three values corresponding with structural differences observed by the pulmonologists. In the case study, I performed binarization manually with a standard thresholding method to delineate structure of interest (SOI) from background and unimportant structures for diagnostic decision (henceforth summarized as just 'background'). To fully automate the workflow in the following publication, I instead used a machine learning approach for this step.

1.2.2.1 Automatic Segmentation - Own contribution

In the presented publication, 'Automated evaluation of Probe-based Confocal Laser Endomicroscopy in the lung' I used a machine learning model for pixel classification (67) to categorize all pixels in every selected snapshot into SOI or background. Machine learning builds a mathematical function based on training samples to make future predictions on test samples. The samples in this case were pixels in manually selected areas, called labels. Labelling was performed with the help of pulmonologists with experience of pCLE examination and DPLD diagnosis. I tested several classifiers with k-fold validation (68) to ensure an optimal choice of classifier. From this evaluation, random forest yielded the highest receiver operating characteristics (69). Random forest uses a collection of nonparametric statistical models called decision trees. The trees provide a solution to difficult decision problems where there are many classes and many available features related in a complex manner (70). The random forest in turn lets multiple trees generate a solution and uses their ensemble 'vote' to make a decision (71). By controlling the voting process of the trees, for instance through sectioning the trees

randomly (72), the method can minimize negative aspects of the process such as decision bias by the trees as a group. However, distribution of the data between selected classes can introduce bias to a models decision process (73, 74). Several techniques exist for overcoming imbalanced class problems (75–77). I selected under-sampling of the overrepresented class for this solution, due to its direct approach and computational efficiency compared to other methods. I selected an initial set of 205 image processing features to train the model. The features were generated by processing the images through different types of image filters, which quantifies pixels' individual appearances as well as their connection to their surroundings. Filters were obtained from a standard 2D-library (containing filters such as 'median', 'gaussian', 'entropy' and 'neighbouring pixel') (78). To select relevant features and exclude the superfluous ones has the outmost importance when training a classification model (79). Thus, I applied a method for selecting features based on minimal redundancy and maximum relevancy (MRMR) (80–82) yielding 84 final features.

1.2.2.2 Structural Quantification - Own contribution

To perform the quantification, a skeleton of the segmented structure was firstly extracted. I generated the skeleton by applying a thinning algorithm that leaves behind a single line of pixels, situated in the objects approximate mid-section (65). The algorithm further ensures that no connected parts are broken up. I then calculated structural connectivity on the skeleton, which quantifies the number of holes in a structure scaled with the skeleton's length. The number of holes were quantified with the Euler number of a binary image. This solution considers patterns of convexity and concavity in local 2-by-2 neighbourhoods as it counts the holes (65). I calculated the local thickness by estimating the distances between individual approximated midpoints from the skeleton and their closest edge pixel from the binary segmentation. I found the closest edge pixels by a k-nearest neighbour search (83) and comparing their the Euclidean distance.

1.3 MRI

MRI uses the concept of the nuclear magnetic resonance (NMR) phenomenon, first described experimentally by both Bloch and Purcell in 1946 (84, 85). The rapid development toward a clinical application has ensured that it is now a widely available, powerful clinical tool accessible in most hospitals (86, 87). However, lung MRI remains a difficult task, due to the intricate structure of the lung as well as their low proton density. This section will firstly focus on the principles of MRI, followed by highlighting problems and efforts of MRI in the lungs. This will lead to the presented work which addresses the issue of variable ventilation and perfusion frequency during the functional evaluation of the lungs.

1.3.1 Magnetic Resonance Imaging

MRI makes use of the quantum magnetic spin property (I) of elementary particles to generate electromagnetic signals. To induce these signals a strong constant magnetic field is applied in one direction B_0 , followed by sequences of pulsed oscillating magnetic fields (radiofrequency (RF) pulses). These RF pulses excite particles with matching, resonant magnetic spin frequency. In turn, the excited particles themselves start to induce an electromagnetic RF signal (88), which can be recorded using receiver coils. By applying specialized sequences of RF pulses and magnetic gradient fields both strength and location of the signal excitation can be manipulated, facilitating the reconstruction of tomographic images of the human body. This introduction will offer only a short overview on the fundamentals of MRI. For a detailed review, the reader is referred to standard textbooks introducing MRI (89, 90).

1.3.1.1 Magnetic spin

The concept of a particle generating a RF signal can be understood by exploring the simplest example, the hydrogen nucleus ^1H , i.e. proton. Protons are the most used nuclei for deriving MR signal due to their high prevalence in the human body (mostly in water molecules). All atomic nuclei are characterized by their atomic number Z (amount of protons), mass number A (total number of protons and neutrons in the nucleus) and nuclear spin I (determined by their intrinsic spin quantum number S , which in turn depends on the numbers of protons and neutrons in a given nucleus). I (equal to $\frac{1}{2}$ for protons) is an intrinsic form of particle angular momentum described by quantum mechanics and connected to the magnetic moment $\boldsymbol{\mu}$ of the nucleus:

$$\boldsymbol{\mu} = \gamma \mathbf{I}, \quad [1]$$

where γ is the particle-specific gyromagnetic ratio.

1.3.1.2 Magnetic macro spin in an external magnetic field

For a single proton inside the magnetic field $\mathbf{B} = B_0 \mathbf{e}_z$ the time-derivative of the magnetic moment $\boldsymbol{\mu}$ can be described classically by:

$$\frac{d\boldsymbol{\mu}}{dt} = \gamma \boldsymbol{\mu} \times \mathbf{B}, \quad [2]$$

which further insinuates that $\boldsymbol{\mu}$ precesses with the Larmor frequency ($\omega_0 = \gamma |\mathbf{B}|$) about the external magnetic field \mathbf{B} . Without an external magnetic field, a collective of uniformly distributed proton spins will be directed in random orientations spatially (due to thermal motion) and produce a net magnetization of zero magnitude. But, as \mathbf{B} is applied on the proton nuclei, individual magnetic

moments will be weakly slanted by their direction. This results in a non-zero expectation value $\langle \mu_z \rangle$ along the direction of the magnetic field. The angular distribution of the magnetic momentum obeys the Boltzmann statistics (91):

$$P(\theta) = \frac{\exp(-E(\theta)/kT)}{\int_0^\pi \exp(-\frac{E(\theta)}{kT}) \sin\theta d\theta}, \quad [3]$$

where the energy difference between two populations of spins is $E(\theta) = -\mu B \cos\theta$ and θ represents the angle between the magnetic moment $\boldsymbol{\mu}$ and the magnetic field \mathbf{B} . With this in mind, $\langle \mu_z \rangle$ can be calculated as

$$\langle \mu_z \rangle = \int_0^\pi P(\theta) (\mu \cos \theta) \sin\theta d\theta \cong \frac{\hbar^2 \gamma^2 B_0}{4kT}. \quad [4]$$

The above approximation is valid when thermal energies are high enough to render quantum effects negligible, or in other words during small degrees of polarization. This is true when $kT > \gamma \hbar B_0$, which for B_0 in standard MRI (between 0.3-3T) is fulfilled at room temperature. It should be said that $\langle \mu_z \rangle$ only describes a mean of expected outcomes in magnetization measurements even for single protons. However, given the classical description of a single nucleus magnetic moment above, the macro-net magnetization $\mathbf{M} = M_0 \mathbf{e}_z$ can also be described by multiplying $\langle \mu_z \rangle$ with number of spins N_s in the measured volume. Similar to the one proton example, the temporal evolution $\mathbf{M}(t)$ of a collective of proton nuclei in a magnetic field $\mathbf{B}(t)$ can be described with

$$\frac{d\mathbf{M}(t)}{dt} = \gamma \mathbf{M}(t) \times \mathbf{B}(t), \quad [5]$$

where the transverse component of the net magnetization will precess with frequency ω_0 around $\mathbf{B}(t)$ as excitation is induced (see below). It is the precession of the transverse component that generates a signal via induced electromotive force in the receiver coils at the same frequency.

1.3.1.3 Excitation and Relaxation

When a RF pulse $\mathbf{B}_1(t) = B_1 [\cos(\omega_0 t), \sin(\omega_0 t), 0]$ pushes the protons already affected by a constant magnetic field $= B_0 \mathbf{e}_z$, $\mathbf{M}(t)$ will be pushed away from equilibrium magnetization ($\mathbf{M} = M_0 \mathbf{e}_z$) into the transverse plane. It will subsequently precess around \mathbf{B} at ω_0 until nearby proton interactions yield relaxation back to equilibrium. Generally, $B_1(t)$ is much weaker in amplitude compared to B_0 and would not affect the net magnetization. But by applying RF pulses matching ω_0 , a resonance effect is achieved resulting in a slow rotation of the net magnetization \mathbf{M} away from the

equilibrium. The total flip angle α of the net magnetization caused by \mathbf{B}_1 will depend on its amplitude B_1 , duration Δt and γ :

$$\alpha = \gamma B_1 \Delta t. \quad [6]$$

Following excitation, relaxation of magnetization occurs both in longitudinal and transverse direction at different time rates. Longitudinal magnetization (M_z) exponentially approaches initial net magnetization M_0 on a timescale T_1 and is dependent on spin lattice interaction (i.e. energy that is released by relaxation is absorbed by the lattice). Transverse magnetization (M_{xy}) decreases exponentially on a timescale T_2 and is dependent on the decay of phase coherence that is obtained immediately after \mathbf{B}_1 . However, generally decay of transverse magnetization is faster than T_2 relaxation due to magnetic field inhomogeneities. This results in further distortion of the spin-spin phase coherence. This effect is accounted for by the additional time factor T_2' and the total decay of transverse magnetization is described by the combined time scale T_2^* , where

$$\frac{1}{T_2^*} = \frac{1}{T_2} + \frac{1}{T_2'}. \quad [7]$$

It should be noted that the additional effect accounted for by T_2' is reversible using a 180° refocusing pulse (see section 1.3.1.4). Specific relaxation times T_1 and T_2 are tissue dependent and vary greatly based on macromolecules within the cells (92), which results in contrast in the final MR image. Similarly, different diseases effect macromolecular environments as well, resulting in total MR signal difference. Empirically the relaxation process in all directions can also be described by the Bloch equations (84):

$$\frac{dM_x}{dt} = \gamma(\mathbf{M} \times \mathbf{B}) - \frac{M_x}{T_2}, \quad [8]$$

$$\frac{dM_y}{dt} = \gamma(\mathbf{M} \times \mathbf{B}) - \frac{M_y}{T_2}, \quad [9]$$

$$\frac{dM_z}{dt} = \gamma(\mathbf{M} \times \mathbf{B}) - \frac{M_0 - M_z}{T_1}. \quad [10]$$

In the case of a constant and homogenous external magnetic field $\mathbf{B} = (0, 0, B_0)$ the solution for M_z is given by:

$$M_z(t) = M_0 - (M_0 - M_z(0))e^{-t/T_1}, \quad [11]$$

and by introducing the complex notation $M_{xy} = M_x + iM_y$, the solution of the Bloch equations for the transverse magnetization is given by:

$$M_{xy}(t) = M_{xy}(0)e^{i\omega t} e^{-t/T_2}. \quad [12]$$

1.3.1.4 Echo generation

In the previous section it was noted that the T_2' -relaxation can be reversed by applying a 180° refocusing pulse. T_2' -relaxation is due to additional local field inhomogeneities caused by magnetic interference fields (or changes in susceptibility at surface boundaries). These constant local field inhomogeneities cause spatially dependent frequency variations of spins rotations, leading to accumulated phase delay. By applying a single 180° pulse at a predefined delay following the initial 90° RF pulse, the spins eventually rephase at twice the original delay time. Since, the signal is read at the time of rephasing, this technique is known as a spin echo and is one of several solutions for phase refocusing. Other multi echo sequences are also readily available, when for example short time to refocus is essential.

1.3.1.5 Spatial localization and k-space

When a signal is recorded, contributions from the entire excited volume are measured. To reconstruct the final MR image it is necessary to separate and spatially assign all contributions. One example to achieve this would be to overlay a linear magnetic gradient field $G_z(\mathbf{x}, t) = \mathbf{x} \cdot \mathbf{g}(t)$, with the magnetic field gradient $\mathbf{g} = \nabla G_z = (\frac{\delta G_z}{\delta x}, \frac{\delta G_z}{\delta y}, \frac{\delta G_z}{\delta z})$ onto $\mathbf{B}=(0,0, B_0)$, and thus spatially modulate \mathbf{B} . Consequently, the total magnetic field strength in z direction will be given by

$$B_z(\mathbf{x}, t) = B_0 + G_z(\mathbf{x}, t), \quad [13]$$

and the Larmor frequency will be spatially dependent:

$$\omega(\mathbf{x}, t) = \gamma B_0 + \gamma \mathbf{x} \cdot \mathbf{g}(t). \quad [14]$$

Neglecting relaxation effects in our example, the transverse magnetization after excitation can be written as:

$$M_{xy}(\mathbf{x}, t) = \rho(\mathbf{x}) e^{i\varphi(\mathbf{x}, t)} M_{xy}(0), \quad [15]$$

where $\rho(\mathbf{x}) = N/V$ is the spatially varying spin density and $\varphi(\mathbf{x}, t)$ is a spatially dependent phase of the transverse magnetization that accumulated in $B_z(\mathbf{x}, t)$. Similar as in [6] $\varphi(\mathbf{x}, t)$ can be calculated from:

$$\begin{aligned} \varphi(\mathbf{x}, t) &= \gamma \int_0^t \omega(\mathbf{x}, \tau) d\tau, \\ &= \omega_0 t + \gamma \mathbf{x} \int_0^t \mathbf{g}(\tau) d\tau, \end{aligned}$$

$$= \omega_0 t + \mathbf{x}\mathbf{k}(t), \quad [16]$$

where the spatial wave vector $\mathbf{k}(t) = \gamma \int_0^t d\tau \mathbf{g}(\tau)$ defines the spatial frequency. The recorded signal $S(t) = S(\mathbf{k}(t))$ is proportional to the spatial average of the transverse magnetization and integration over the volume V results in:

$$S(t) \propto \int_V M_{xy}(\mathbf{x}, t) d^3\mathbf{x} = M_{xy}(\mathbf{x}, 0) \int_V \rho(\mathbf{x}) e^{i\mathbf{x}\mathbf{k}(t)} d^3\mathbf{x}. \quad [17]$$

Thus, apart from a scaling factor, it equals the value of the Fourier transform of $\rho(\mathbf{x})$ at $\mathbf{k}(t)$. Since $\mathbf{g}(t)$ determines k-space points $\mathbf{k}(t)$, $S(\mathbf{k})$ can be measured for arbitrary k . Furthermore, if $S(\mathbf{k})$ is measured in a sufficient number of points \mathbf{k} , $\rho(\mathbf{x})$ can be approximated with inverse discrete Fourier transform, since:

$$\rho(\mathbf{x}) \propto \sum_p S(\mathbf{k}_p) e^{-i\mathbf{k}_p \mathbf{x}}. \quad [18]$$

Oftentimes in MRI, $S(\mathbf{k})$ is measured in a zero-centred grid of equidistantly spaced points \mathbf{k}_i (where $i = -N \dots (N - 1)$), called k-space. $\rho(\mathbf{x})$ can in that case be approximated with:

$$\rho(\mathbf{x}) = C \sum_{n=-N}^N S(n\Delta k) e^{-in\Delta k \mathbf{x}}, \quad [19]$$

where Δk is the distance between two point and determines field of view (FOV) of the final image ($FOV = 2\pi/\Delta k$). The spatial resolution Δx of an image can through this also be obtained, since $\Delta x = FOV/2N = \pi/N\Delta k$.

1.3.1.6 Slice selection

Although spatial assignment can be performed directly on a 3D-volume, a common separate step called slice selection is often applied to reduce the 3D reconstruction to 2D. This is performed by only exciting protons within a predefined slice with the applied RF pulses and involves two subsequent steps:

- 1) A magnetic field gradient applied perpendicular to the plane of the selected slice, resulting in a linear variation of resonance frequencies along the field direction.
- 2) An applied short RF pulse, which is specifically tailored to match the narrow range of frequencies contained in the selected slice.

The thickness and profile of the selected slice will depend on the envelope, amplitude, frequency bandwidth of the applied RF pulse. This ensures that subsequent sampling only must take place in two remaining dimensions.

1.3.1.7 K-space sampling and image reconstruction

Since the value of $\mathbf{k}(t)$ is dependent on the time integral over which $\mathbf{g}(t)$ is applied, appropriate choice of gradient fields can select a specific value of $\mathbf{k}(t)$ and thus measure $S(\mathbf{k})$ at arbitrary points in k-space. After the above slice selection step for example, k-space is traversed in a 2-D by activating (g_x, g_y) for (t_x, t_y) amount of time to locate the specific positions (k_x, k_y) in k-space. This is followed by a readout gradient that collects signals points while k-space is traversed.

1.3.1.8 Sequences

To perform MR imaging a specific combination of the excitation, possibly refocusing pulses, spatial encoding, echo generation and signal acquisition is applied, which altogether is referred to as a pulse sequence. By varying these factors, specific contrast in brightness between tissue can be yielded. Particularly selection of repetition time (TR), echo time (TE) and the flip angle α have a strong influence on the contrast and how the image will be weighted. The TR is simply the time between two RF pulses and the TE the time between the application of a RF pulse and the recording of the signal.

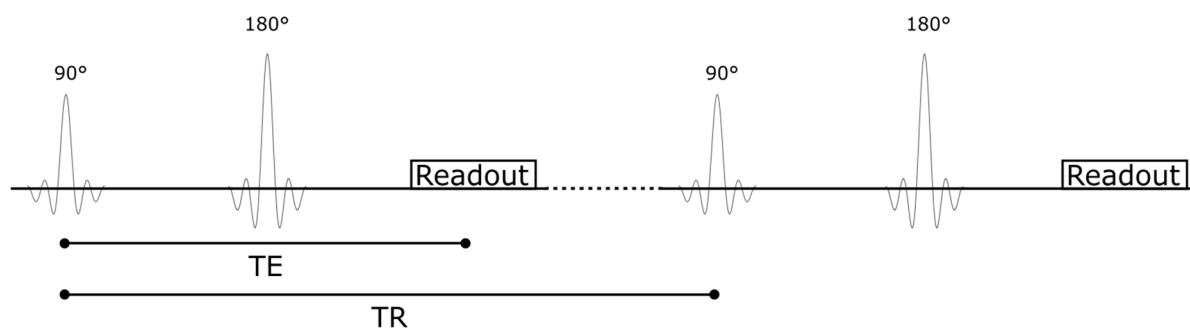


Figure 1: Diagram of RF and readout deciding TR and TE . In the example, the 180° refocusing pulse occurs at $t=TE/2$.

As previously established, following excitation, M_z returns to M_0 at relaxation rate T_1 and M_{xy} returns to 0 at relaxation rate T_2 . However, T_1 and T_2 are tissue dependent, which can be exploited to generate contrast between organs and tissues in the reconstructed images. This is achieved by using specific combinations of the sequences parameters TE and TR as follows: Generally speaking, short TR values (less than 300ms) lead to a T_1 -weighted image contrast and long TE -values (longer than 90ms) lead to a T_2 -weighted image contrast (since these values enhance the relaxation effects on the transversal magnetization at the time of the signal readout). In contrast, long TR - (longer than 1000ms) and short TE (shorter than 15ms) will instead suppress both T_1 and T_2 relaxation effects, and the image contrast will mostly be based on local proton densities from the volume.

1.3.2 MRI of the Lungs

MRI measurements in the lungs are difficult due to low proton density, short T_2^* relaxation time and motion artefacts. Proton density of the lungs has been measured to be between 1/10 and 1/5 of other human tissues, depending on ventilation phase, subject position and measurement localization (93, 94). This translates to a much lower signal-to-noise ratio (SNR) from lung parenchyma compared to other tissue types. The short T_2^* relaxation time is due to the complex structure of the lungs. The transitions between tissue and air result in magnetic susceptibility gradients (95) and with very small structures compared to voxel size, the signal suffers particularly fast T_2^* dephasing. Thus imaging the lungs requires pulse sequences with TE as short as ideally 1-2ms (96). T_2^* dephasing is even faster at higher magnetic field strengths (97) leading to a weigh-off between the SNR gain due to higher magnetization vs. further shortening of T_2^* .

1.3.2.6 *Balanced steady state free precession MR sequence*

A balanced steady-state free-precession (bSSFP) sequence generates a steady-state signal by refocusing the remaining transverse magnetisation after readout of the signal. It does so by applying additional pulses with alternating phases (flipped polarity) at the end of every TR interval (98). Consequently, the generated signal will be proportional to the ratio T_2/T_1 for all TR that fulfils the condition $TR \ll T_1, T_2$ (99). With optimised implementation to compensate banding artefacts (100) and using state of the art hardware, bSSFP has been shown to be feasible with TR as low as 3 ms. By sacrificing spatial resolution, bSSFP sequences have been shown to acquire up to 5 MRI slices per second (8), enabling the tracking of ventilation and perfusion related signal changes. bSSFP sequences also have the added advantage of offering intrinsic flow compensation along both phase and slice direction for 2D imaging (101, 102).

1.3.2.7 *Fourier decomposition MRI*

Fourier decomposition (FD) MRI is a free-breathing and non-contrast enhanced post-processing method applied on dynamic MRI image series to evaluate functional pulmonary information in the lung. During inhalation the lung expansion translates to a decreased amount of tissue per voxel, which lowers the proton density and connects signal variations with the breathing cycle (103). Blood perfusion is similarly connected to proton density due to capillary blood filling as well as intravoxel dephasing (7). The initial implementation of FD MRI acquires time-resolved 2D-MR images series with the bSSFP sequence. By non-rigidly registering all lung images to a mid-ventilation phase reference image, signal variations of lung regions are connected to specific voxels (104, 105). Signal variation over the whole time series can then be extracted from every voxel and their frequency content evaluated with a 1D-fast Fourier transform (FFT) in the temporal dimension. The spectral images are then separated into perfusion- and

ventilation-weighted functional maps based on their frequency content, yielding the relative amplitude and phase of both signals. Ventilation usually resides in frequency bands below 0.5 Hz and perfusion frequency over 0.75 Hz. Accordingly, they can be distinguished if the acquisition frequency overcomes the Nyquist-Shannon limit (106) and the spectral resolution is sufficiently high to distinguish frequency peaks.

The amplitude maps' feasibility to spot localized lung pathologies has already been highlighted in multiple studies (8–10) as well as the possibility to generate V/Q maps simultaneously (107). The phase information yielded from FD has also been suggested to yield relative estimates of signal arrival time between voxels. This could potentially highlight localized signal delays caused by pathologies (108, 109). However, attention has been raised, that frequency variability of both ventilation and perfusion signals during image acquisition can result in problems for the accuracy with FD (110). FFT assumes constant frequency over a full measurement, which during any free breathing measurement is close to non-existent. A natural variability in frequency can always be expected in both signal variations even in the healthy subjects. However, particularly in patients with obstructed or restricted breathing, specifically high variations can be expected exacerbating the issue. This translates to inaccurate amplitude and phase maps generated by the FFT.

1.3.3 Non-uniform Fourier decomposition MRI for ventilation and perfusion weighted imaging of the lung – Own contribution

Two methods were initially introduced to account for frequency variability, by resorting multiple signal variations into an average single frequency ventilation cycle. However, these were complex multi-step methods utilizing exact phase estimation, peak finding and data resorting of image-(46) or k-space (111). The presented method, Non-uniform Fourier decomposition (NUFD) on the other hand, aimed to use the simplistic concept of standard FD while still accounting for the frequency variability.

NUFD assumes only the following:

- An equidistantly sampled oscillating signal with variable frequency can be reinterpreted as a non-equidistantly sampled signal with constant frequency.
- Frequency variations for ventilation and perfusion in the lungs are consistent between voxels.

I implemented this reinterpretation, by calculating new virtual non-equidistant time points, which compensates for the signal's frequency variation. The virtual time points were calculated with a frequency-tracking step, yielding a correction factor. To estimate the frequency content of a non-equidistantly spaced signal I used the non-uniform FFT (112) (NUFFT) instead of FFT, which will be

introduced in the following section. The final workflow, that I developed to generate ventilation- and perfusion-weighted NUFD maps can be summarized in the following steps:

1. Perfusion and ventilation signals are extracted from a selected region of interest in the registered lung segments
2. Frequency of perfusion and ventilation signals are tracked in the same time-frequency estimation using two ridges, with a penalty for jumping between peaks to avoid cross tracking.
3. New virtual time points are calculated to compensates the signals' frequency variation.
4. The virtual time points were used for NUFFT in every pixel and ventilation and perfusion maps spectrally separated.

Furthermore, SNR estimation of a signal in frequency spectrum is a well-established technique (110). Thus, I could perform a quantitative pixel-to-pixel comparison between generated NUFD and FD maps.

1.3.3.6 Frequency tracking & correction - Own contribution

Tracking frequency over time is a non-trivial task where complexity begins at the initial signal formulation $S(t)$. the standard Fourier transform splits $S(t)$ into distinct sinusoidal components and assumes constant frequency over its full measurement time. If signals are not perfectly sinusoidal and vary in frequency, spectral components will 'spill' out onto other frequency bins resulting in fewer parts of the signal being used for evaluation or even incorrect assessment of its parameters. The continuous wavelet transform (CWT) (114) has been presented as a solution to these issue, by instead describing the transform component as a general function ψ with a scalable window $1/a$. By doing so, it achieves signal descriptions in both time and frequency space:

$$W_x(a, b) = \int_{-\infty}^{\infty} S(t) \frac{1}{a} \psi\left(\frac{t-b}{a}\right) dt, \quad [20]$$

where a and b are called the scale and translational variables, respectively. The CWT also has an inverse formalism to recover the original signal $S(t)$ and by selecting a considered function ψ , multicomponent signals can be incorporated into a single spectral line without interference between each component (114). From the CWT I could then track the combined instantaneous frequency (115) (IF) of the signal by estimating a ridge curve, following the signals' max amplitude in the time-frequency domain (116). the precision of the IF estimate determines how well frequency is collected in the final NUFFT step. The synchro-squeezed wavelet transform collects signal energy with the same phase onto a single frequency bin (117) and have shown to improve frequency localization compared to standard CWT

(118). For this reason, I also applied this to the workflow. With IF estimated, I could calculate new time points at every index n with:

$$\tilde{t}_n = \frac{\Delta t}{f_{mean}} \sum_{k=1}^n f(t_k), \quad [21]$$

where Δt is the time between two time points in the original equidistant time vector, f_{mean} is a scaling factor set to mean value of IF (which ensures that equal total acquisition time between the virtual and original time vector and $f(t_k)$ the instantaneous frequency at time point index k). I then used the non-equidistant time vector as input to a type-1 NUFFT which quantifies frequency components F_k of the new signal $\tilde{S}(\tilde{t})$ through:

$$F_k = NUFFT(S(\tilde{t}_n)) = \sum_{n=1}^N S(\tilde{t}_n) \exp\left(-\frac{2\pi i k \tilde{t}_n}{\tilde{t}_N - \tilde{t}_1}\right). \quad [22]$$

2. Summary/Zusammenfassung

2.1 Automated evaluation of Probe-based Confocal Laser Endomicroscopy in the lung

Probe based confocal endomicroscopy (pCLE) is a novel imaging modality that provides real time videos of autofluorescent elastin structures within the alveoli. Changes in the elastin structure caused by diffuse parenchymal lung diseases (DPLD) can be shown on the captured images. However, these changes are oftentimes moderate and the evaluation of the performing physician relies mainly on the qualitative assessment of individual images selected manually after the examination. The focus of the publication “Automated evaluation of Probe-based Confocal Laser Endomicroscopy in the lung” was to design and implement an automated workflow for the segmentation and quantitative evaluation of pCLE images followed by the analysis of its diagnostic potential to identify DPLDs. For this purpose, I trained and optimized a machine learning model for the automatic segmentation of structures of interest (SOI) in the recorded pCLE images. Furthermore, I developed an algorithm that calculates quantitative values describing the segmented alveolar structures' local thickness statistics and structural connectivity. I then analysed the workflow's diagnostic potential on images from 46 subjects. Images from 38 patients (divided into 4 different DPLD groups) were analysed and compared against 8 subjects with images characterized as normal elastin structure by pulmonologists selecting snapshots. The DPLD groups were cryptogenic organizing pneumonia (COP), non-specific interstitial pneumonia (NSIP), idiopathic pulmonary fibrosis (IPF) and hypersensitive pneumonitis (HP).

The segmentations performed well, extracting SOIs while removing background, as confirmed by cross validation as well as the expert pulmonologist. The quantified structural connectivity, median thickness as well as the standard deviation of thickness showed statistically significant differences in all DPLD groups compared to the normal group ($p < 0.05$). These results indicate that qualitatively described structural changes of alveoli elastin structure caused by different DPLDs (57–60) can be automatically quantified and used to distinguish healthy from diseased tissue using the developed framework. If implemented into the current clinical workflow, the presented method could offer quantitative evaluation of selected pCLE images, decreasing variability compared to current qualitative assessments and potentially offer real-time diagnostic confirmation of suspected DPLD structures.

Die Sonden-basierte, konfokale Endomikroskopie (pCLE) ist eine neuartige Bildgebungsmodalität, die die Aufnahme von Echtzeitvideos von autofluoreszierenden Elastinstrukturen in den Alveolen ermöglicht. Auf den erfassten Bildern können sich Änderungen der Elastinstruktur darstellen, die durch diffuse parenchymale Lungenerkrankungen verursacht werden. Diese Änderungen sind jedoch häufig moderat und die Befundung des durchführenden Arztes beruht hauptsächlich auf einer qualitativen Beurteilung einzelner Bilder, die nach der Untersuchung manuell ausgewählt werden. Der Schwerpunkt der Veröffentlichung „Automated evaluation of Probe-based Confocal Laser Endomicroscopy in the lung“ lag auf dem Entwurf und der Implementierung eines automatisierten Workflows zur Segmentierung und Auswertung der ausgewählten pCLE-Bilder, gefolgt von der Analyse des diagnostischen Potenzials zur Identifizierung von DPLDs. Hierzu habe ich zunächst ein Machine Learning Modell trainiert und optimiert, welches zu untersuchende Strukturen in den aufgenommenen pCLE Bildern automatisch segmentiert. Darüber hinaus habe ich einen Algorithmus entwickelt, welcher Statistik der lokalen Dicken und die strukturelle Konnektivität der segmentierten Alveolarstrukturen quantifiziert. Anschließend analysierte ich das diagnostische Potenzial des Workflows anhand von Bildern von 46 Untersuchungen. Insgesamt wurden Aufnahmen von 38 Patienten (mit vier verschiedenen DPLDs) analysiert und mit Aufnahmen von 8 weiteren Patienten verglichen, deren Elastinstruktur von den durchführenden Pneumologen als normal charakterisiert wurden. Die untersuchten DPLDs umfassten die kryptogene organisierende Pneumonie (COP), die unspezifische interstitielle Pneumonie (NSIP), die idiopathische Lungenfibrose (IPF) und überempfindliche Pneumonitis (HP).

Sowohl das Kreuzvalidierungsverfahren als auch die visuelle Beurteilung eines erfahrenen Pneumologen bestätigten die gute Leistung der automatischen Segmentierungen der Elastinstrukturen. Die quantifizierte strukturelle Konnektivität, der mittlere Durchmesser sowie die Standardabweichung des Durchmessers zeigten statistisch signifikante Unterschiede in allen DPLD-Gruppen im Vergleich

zur normalen Gruppe ($p < 0,05$). Diese Ergebnisse zeigen, dass zuvor qualitativ beobachtete strukturelle Veränderungen der Alveolenelastinstruktur, die durch verschiedene DPLDs verursacht werden (57–60), mithilfe des entwickelten Workflows vollautomatisch quantifiziert und von einer gesunden Elastinstruktur unterschieden werden können. Bei Implementierung in den aktuellen klinischen Arbeitsablauf könnte die vorgestellte Methode ausgewählte pCLE Aufnahmen quantitativ auswerten, die Variabilität im Vergleich zur aktuellen qualitativen Bewertungen verringern und potentiell eine Bestätigung in Echtzeit für die Diagnose von pathologischen Elastinstrukturen bieten.

2.2 Non-uniform Fourier decomposition MRI for ventilation and perfusion weighted imaging of the lung

Fourier decomposition (FD) MRI is a non-invasive free breathing imaging processing method, used on lung image series for extracting local functional information about ventilation and perfusion. However, naturally occurring respiratory and cardiac frequency variations during image acquisition may corrupt the estimations. Thus, the focus of the publication “Non-uniform Fourier decomposition MRI for ventilation and perfusion weighted imaging of the lung” was to address signals’ frequency variation and consequently increase the robustness of pulmonary ventilation- and perfusion-weighted imaging. This was achieved by a two-step approach, where the first step entailed reinterpreting the equidistantly sampled varying-frequency signals to non-equidistantly sampled signals with constant frequency. For this, I reinterpreted the recorded signal by scaling the original measurement time points with their individual instantaneous frequencies. The signal’s instantaneous frequency was thereby tracked using a wavelet transform. For the second step I analysed the resulting non-equidistantly sampled signals with non-uniform Fourier decomposition (NUFD) to generate perfusion- and ventilation-weighted maps. I compared the developed NUFD workflow against standard FD by evaluating the signal-to-noise ratio (SNR) from the generated ventilation and perfusion maps of 11 patients and 5 healthy test subjects. This showed that the NUFD significantly increased average SNR in ventilation and perfusion for both groups ($p < 0,05$). The maximum SNR increase in one test subject was 144.0% and in two CTEPH patients, the implemented NUFD method recovered perfusion signals which could not be analysed with standard FD. These results show that accounting for frequency variability, NUFD truly offers a free-breathing method with broad applicability. The frequency tracking step ensures that even patients with breathing difficulties and/or strong arrhythmia can be included in examinations. Furthermore, the NUFD framework can be readily applied to current and past FD studies as it requires no changes to the image acquisition parameter.

Die Fourier-Decomposition-MRT (FD) ist eine nicht-invasive Methode bei freier Atmung, die anhand von zeitlich aufgelösten Bildserien der Lunge Informationen über die lokale Ventilation und Durchblutung des Lungenparenchyms in Form von Parameterkarten gewinnen kann. Häufig auftretende

Schwankungen der Atem- und Herzfrequenz während der Bildaufnahme können jedoch die berechneten Ergebnisse verfälschen. Daher lag der Schwerpunkt der Veröffentlichung „Non-uniform Fourier decomposition MRI for ventilation and perfusion weighted imaging of the lung“ darin, die Frequenzschwankungen zu analysieren und zu korrigieren um damit die Robustheit und Genauigkeit der gewonnenen Information über Ventilation und Perfusion zu verbessern.

Dies wurde durch einen zweistufigen Ansatz erreicht, bei dem im ersten Schritt die zeitlich äquidistant abgetasteten Signale mit schwankender Frequenz in nicht äquidistant abgetastete Signale mit konstanter Frequenz reinterpretiert wurden. Dazu habe ich die ursprünglichen Messzeitpunkte des Signals mit der individuellen Momentanfrequenzen skaliert. Die zeitaufgelöste momentane Frequenz des Signals wurde dabei unter Verwendung einer Wavelet-Transformation bestimmt. Für den zweiten Schritt analysierte ich die resultierenden, nicht äquidistant abgetasteten Signale mit der „Non-uniform Fourier decomposition“ (NUFD), um die perfusions- und ventilationsgewichteten Karten zu erstellen. Ich verglich die entwickelte NUFD-Methode mit der für gewöhnlich verwendeten standard Fourier Zerlegung, indem ich das Signal-Rausch-Verhältnis (SNR) aus den generierten Ventilations- und Perfusionskarten von 11 Patienten und 5 gesunden Probanden auswertete. Die Ergebnisse zeigten, dass die entwickelte NUFD-Methode das durchschnittliche SNR der Ventilations- und Perfusionskarten in beiden Gruppen signifikant erhöhte ($p < 0,05$). Der höchste SNR-Anstieg bei einem Probanden lag bei 144,0%, und bei zwei CTEPH-Patienten ermöglichte die NUFD-Methode die Analyse von Perfusionssignalen, die mit der standard Fourier Zerlegung nicht messbar waren. Diese Ergebnisse verdeutlichen, dass die NUFD-Methode mit Berücksichtigung der Frequenzschwankungen ein Verfahren mit breiter Anwendbarkeit bei echt freier Atmung bietet. Die Berücksichtigung der Frequenzschwankungen stellt sicher, dass auch Patienten mit Atembeschwerden und / oder starker Arrhythmie untersucht werden können. Darüber hinaus kann die NUFD-Methode problemlos auf aktuelle und bereits abgeschlossene Studien mit Fourier Zerlegung angewendet werden, da keine Änderungen am Aufnahmeprotokoll der MRT Bilder erforderlich sind.

3. Original publications

- 3.1 Bondesson D, Schneider MJ, Silbernagel E, Behr J, Reichenberger F, Dinkel J (2020) Automated evaluation of probe-based confocal laser endomicroscopy in the lung. PLoS ONE 15(5): e0232847. <https://doi.org/10.1371/journal.pone.0232847>**

RESEARCH ARTICLE

Automated evaluation of probe-based confocal laser endomicroscopy in the lung

David Bondesson^{1,2*}, Moritz J. Schneider^{1,2}, Edith Silbernagel³, Jürgen Behr^{3,4}, Frank Reichenberger³, Julien Dinkel^{1,2,5}

1 Department of Radiology, University Hospital, LMU Munich, Munich, Germany, 2 Comprehensive Pneumology Center (CPC-M), University Hospital, LMU Munich, Helmholtz Zentrum München, Member of the German Center for Lung Research (DZL), Munich, Germany, 3 Department of Pneumology, Asklepios Fachklinikum Munich-Gauting, Member of the German Center for Lung Research (DZL), Munich, Germany, 4 Department of Internal Medicine V, University of Munich (LMU), Munich, Germany, 5 Department of Radiology, Asklepios Lung Center Munich-Gauting, Munich, Germany

* david.bondesson@med.uni-muenchen.de

Abstract

Rationale

Probe-based confocal endomicroscopy provides real time videos of autofluorescent elastin structures within the alveoli. With it, multiple changes in the elastin structure due to different diffuse parenchymal lung diseases have previously been described. However, these evaluations have mainly relied on qualitative evaluation by the examiner and manually selected parts post-examination.

Objectives

To develop a fully automatic method for quantifying structural properties of the imaged alveolar elastin and to perform a preliminary assessment of their diagnostic potential.

Methods

46 patients underwent probe-based confocal endomicroscopy, of which 38 were divided into 4 groups categorizing different diffuse parenchymal lung diseases. 8 patients were imaged in representative healthy lung areas and used as control group. Alveolar elastin structures were automatically segmented with a trained machine learning algorithm and subsequently evaluated with two methods developed for quantifying the local thickness and structural connectivity.

Measurements and main results

The automatic segmentation algorithm performed generally well and all 4 patient groups showed statistically significant differences with median elastin thickness, standard deviation of thickness and connectivity compared to the control group.

OPEN ACCESS

Citation: Bondesson D, Schneider MJ, Silbernagel E, Behr J, Reichenberger F, Dinkel J (2020) Automated evaluation of probe-based confocal laser endomicroscopy in the lung. PLoS ONE 15(5): e0232847. <https://doi.org/10.1371/journal.pone.0232847>

Editor: David Mayerich, University of Houston, UNITED STATES

Received: February 6, 2020

Accepted: April 22, 2020

Published: May 6, 2020

Copyright: © 2020 Bondesson et al. This is an open access article distributed under the terms of the [Creative Commons Attribution License](https://creativecommons.org/licenses/by/4.0/), which permits unrestricted use, distribution, and reproduction in any medium, provided the original author and source are credited.

Data Availability Statement: All relevant data are within the manuscript and its Supporting Information files.

Funding: The author(s) received no specific funding for this work.

Competing Interests: The authors have declared that no competing interests exist.

Conclusion

Alveoli elastin structures can be quantified based on their structural connectivity and thickness statistics with a fully-automated algorithm and initial results highlight its potential for distinguishing parenchymal lung diseases from normal alveoli.

Introduction

Diagnostics of diffuse parenchymal lung disease (DPLD) is to this day a complex task performed using the collective information from clinical, radiological and histological criteria and analysed in a multidisciplinary discussion [1–3].

However, even gold standard imaging methods such as high resolution computer tomography (HRCT) [4,5] struggle to yield consensus with regards to diagnosis in DPLD with a large interreader variability [5], advocating a need for additional diagnostic information in equivocal cases [6]. For this reason, pathological specimens are sometimes necessary in the diagnostic workup, such as surgical lung biopsy and more recently bronchoscopic cryobiopsy [7]. However, invasive tissue sampling methods, risk causing complications such as pneumothorax, haemorrhage and acute exacerbation of the DPLD. To address this issue, probe-based confocal laser endomicroscopy (pCLE) has been presented as a novel technique for providing imaging of the respiratory tract and alveolar ducts in real time [8] based on the microstructures' autofluorescence [9].

Image acquisition is done by introducing the pCLE probe through a flexible bronchoscope during standard examination. The probe captures 12 images/second with the following image parameters: Distal diameter = 1.4 mm, Field of view = 600 μm , imaging depth = 0 – 50 μm , lateral resolution = 3.5 μm , axial resolution = 15 μm . The probe diameter of 1.4 mm ensures that it can be pushed deep into the lung. It emits laser light with a wavelength of 488 nm which excites autofluorescence from the elastin content in the alveoli structures. With a multitude of technical improvements over the last 15 years to overcome the low specificity of autofluorescence defects [10,11], pCLE has shown promise as a diagnostic method to visualize lung tissue in vivo [12,13]. Multiple studies [14–17] have investigated the structural changes of lung tissue caused by different DPLDs and specifically highlighted increased elastin fibre thickness, density of fibres and number of cellular structures as important features. The aim of this study was to develop a fully automatic workflow for quantifying these structural properties using pCLE measurements and to perform a preliminary assessment of their diagnostic potential.

Materials and methods

Patient characteristics

46 patients were included in this study (mean age \pm standard deviation = 70.1 \pm 8.2, 30 male and 16 female, 29 ex-smokers (since more than 10 years), 15 non-smokers and 2 without info). All patients were newly diagnosed in accordance with histological, radiological and clinical results based on a multidisciplinary discussion. Each patient was assessed according to current guidelines including HRCT, biopsy, pulmonary function test with blood gas analysis and 6-minute-walk test. All were referred for examination as part of workup of newly diagnosed DPLD and in stable clinical condition. Of these, 11 were diagnosed with cryptogenic organizing pneumonia (COP), 8 with non-specific interstitial pneumonia (NSIP), 11 with idiopathic pulmonary fibrosis (IPF) and 8 with hypersensitive pneumonia (HP). 5 patients with

Sarcoidosis (without histological lung pulmonary involvement) were classified as normal parenchyma. Additionally, pCLE was performed on the contralateral healthy lung of one patient with an allergic bronchopulmonary aspergillosis as well as one with bronchial pneumonia. HRCT showed no abnormality in these unaffected lungs. Lastly, pCLE was performed on a patient with metastases from breast cancer in unaffected parts of the lung. Altogether, this made for 8 patients classified as having normal elastin structure. Exclusion occurred based on severe restriction (vital capacity or total lung capacity below 50% pred.), severe hypoxaemia ($pO_2 < 55$ mmHg), congenital or acquired disorder of the coagulation system, signs of pulmonary hypertension, signs of infection, exacerbation or inability to undergo bronchoscopy for any medical or legal reason. The study was approved by the local ethics committee of the Ludwig Maximilians University Munich, Germany, (Record number 048/13). All patients obtained information by a pulmonologist and gave their written informed consent to use the pCLE mini probe during the bronchoscopy 24 hours prior to examination.

Image acquisition

The patients underwent bronchoscopy examination in combination with pCLE (Cellvizio, Mauna Kea Technologies, France, Paris) with varying duration. The bronchoscopy examination was performed according to guidelines in rigid technique with patients under general anaesthetic using a flexible bronchoscope (BF-Q 180, Olympus, Japan) to collect mucus samples for microbiological and cytological assessment as well as examine the bronchial tree. Next, the pCLE probe was pushed through the working channel of the bronchoscope and further into the peripheral compartment of the bronchial tree with fluoroscopic guidance until elastin fibres of alveoli ducts were reached. PCLE was performed in regions of the lung which showed clear signs of pathology from the HRCT images. Neighbouring sub-segments were also examined in cases where no obvious pathological structure could be observed. No exogenous fluorophores were required for this procedure. The pCLE recordings were taken during extractive motion of the probe to limit contact pressure of the probe onto the tissue surface. Using Cellvizio Viewer Software v.1.6.0 (Mauna Kea Technologies, Paris, France), snapshots from the recordings that displayed characteristic alveoli elastin structure without elastin tension or procedure related changes were selected by two pulmonologist experienced in interventional rigid bronchoscopy to be quantified (Fig 1A). The pulmonologists were unaware of the results of other performed diagnostic tests.

Image processing

A machine learning model [18] was trained for the fully automatic segmentation. Model training and pixel classification were performed in 'Trainable Weka Segmentation' [19] called from ImageJ (Fiji) [20] as a plugin. 23 snapshots were manually labelled by the pulmonologists (resulting in 267 elastin areas and 232 background areas constituting a total of 1060543-pixel instances). The snapshots were randomly selected resulting in a set of 4 NSIP cases, 15 IPF cases and 2 normal cases. 21 of the snapshots were used for training and tuning the classifier. Since there were approximately 2.5 times more instances of background than elastin structure in the labels, random undersampling [21] was performed to rebalance the classes. Features were generated from a multitude of image filtering methods available in Trainable Weka Segmentation that extract different spatial characteristics from an image. Classifiers were trained on instances with an added correlation-based feature selection step [22] to minimize their intraclass correlation while improving upon prediction accuracy. Features were ranked based on their information gain ratio. The last 2 snapshots (with 77650 instances) were used as a test set for comparing the classifiers. A random forest classifier with 200 trees yielded highest

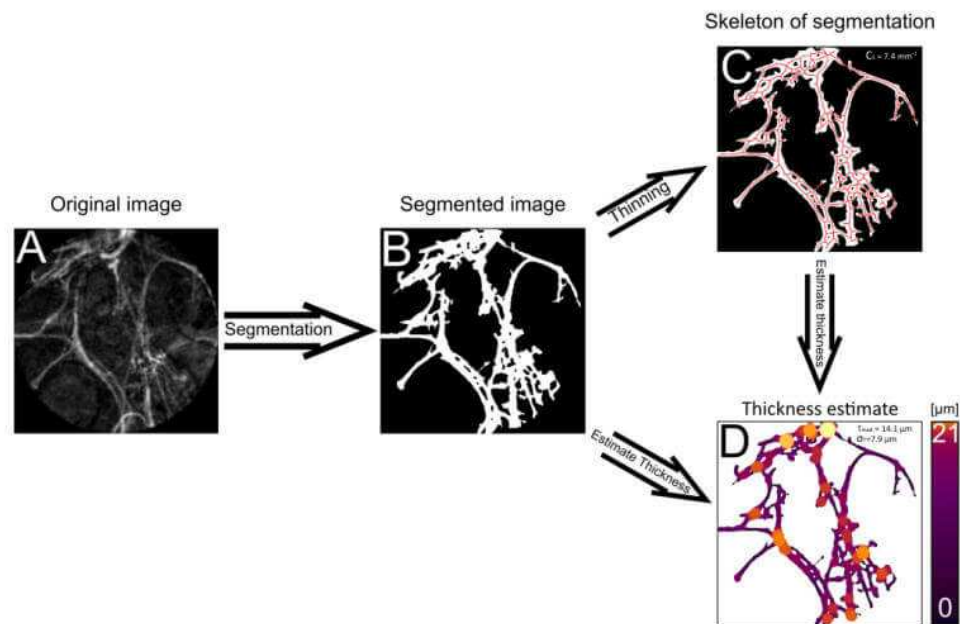


Fig 1. Workflow for structural evaluation of alveoli elastin. A) Example of acquired NSIP patient snapshot from pCLE screening. B) Resulting segmentation generated by pixel classification based on a machine learning approach. C) Generated skeleton of structure used when calculating local thickness. D) Visualization of local thickness for whole structure.

<https://doi.org/10.1371/journal.pone.0232847.g001>

receiver operating characteristics on the test images (area of 98.8% under the curve) and was thus selected for segmentation. A total of 131 representative screenshots from the 46 patients were segmented (Fig 1B) using this model. Representative shots entailed those that showed characteristic elastin structure for pathological or normal healthy structure in accordance with described criteria [14]. The segments were subsequently visually assessed by the two pulmonologists to ensure that elastin structures of interest were included, and background textures removed. In some instances, pixel classification was not able to determine with certainty if some regions were holes or structure and could generate small regions that looked like pixel noise with a mixture of both. To prevent an artificial increase of holes, those with a distance between each other smaller than $2 \mu\text{m}$ were merged and holes smaller than $30 \mu\text{m}$ filled in. Numerical values were chosen empirically by pulmonologists. Due to an imbalanced number of snapshots per patient, only the first snapshot from each examination was processed and used for the statistical evaluation. Due to low signal to noise ratio (SNR) in some acquired snapshots leading to segmentation irregularities, one HP measurement was excluded and in two measurements the second snapshot was instead used for evaluation. The segments were then evaluated based on their structural tissue connectivity C_s (Fig 1C), median and standard deviation of local thickness (T_{med} and σ_T , respectively) (Fig 1D).

Image processing—Connectivity calculation. C_s aimed to detect increases of intricacies in the elastin structure associated with DPLDs by quantifying the number of holes of the segmented elastin structure normalized with respect to the structure's size. Firstly, to estimate a

structure's size, a skeleton was generated by applying a thinning algorithm (skeletonization) [23], creating a one pixel thick topology-preserved medial axis structure (Fig 1C). The skeleton was considered a better value to scale with compared to the binary segmented area, since this was not affected by pixelated edge effects. The number of holes was calculated from the Euler number of the binary snapshots [23]. This quantifies the number of structures and the amount of holes these structures inhibit. C_s was then generated from the number of holes normalized by the total length of the skeleton $L_{skeleton}$.

Image processing—Local thickness estimation. To estimate the local thickness T_{local} of a structure, the distance from the local centre of the structure to the closest edge was used. Since the generated skeleton represents local midpoint estimations, only the distance to the closest neighbouring pixel d_{np} for all skeleton points must be determined. The nearest neighbour pixel was found with a k-nearest neighbour algorithm [24] where the pixel with minimum Euclidean distance was selected. T_{local} was then calculated by doubling d_{np} . Pathology groups were then compared against the characteristically normal group for each parameter resulting in 12 comparisons.

Statistical evaluation

For statistical comparison the Wilcoxon rank sum test (two-tailed) [25] was used. Differences were considered to be statistically significant for p-values of less than 0.05 after applying Bonferroni correction [26] (number of tests = 12).

Results

Image processing

The automatic segmentation algorithm performed well on the patient data in accordance with the pulmonologists' inspection. One HP-patient's snapshots were removed from the evaluation as only small parts of the structure remained after segmentation. Fig 2 depicts three examples of results generated by the alveoli structure evaluation. Fig 2A displays a normal alveoli structure imaged in low SNR with resulting values $T_{med} = 17.2 \mu m$, $\sigma_T = 8.6 \mu m$ and $C_s = 0.4 mm^{-1}$. Fig 2E displays an IPF patient with characteristic distortion and increased intricacies of the alveolar structure. This resulted in higher values than in the normal tissue example: $T_{med} = 37.4 \mu m$, $\sigma_T = 21.4 \mu m$ and $C_s = 5.2 mm^{-1}$. Fig 2I displays an NSIP patient where an apparent large density was observed. The segmented image distinguished the characteristic crystalline coating and included that as a structure to be evaluated. This too resulted in higher calculated values compared to the normal case: $T_{med} = 24.3 \mu m$, $\sigma_T = 11.6 \mu m$ and $C_s = 4.9 mm^{-1}$.

Statistical evaluation

Significant differences were found when comparing the pathological cases against the normal in all of values (Fig 3). When comparing group median of all variables, COP-, HP-, NSIP and IPF- measurements all showed significant increases for T_{med} , σ_T and C_s with $p < 0.05$.

Table 1 summarizes the group median difference of the three values between all pathology snapshots and the normal snapshots. T_{med} differences varied between 4.3 – 12.6 μm ($p < 0.05$). σ_T differences varied between 5.8 – 1.4 μm ($p < 0.05$). C_s differences varied between 1.70 – 3.76 mm^{-1} ($p < 0.05$).

Discussion

We are presenting a follow up study to a previous review article [27], that first suggested a semi-automatic method for the structural evaluation of alveoli elastin. Comparatively, this

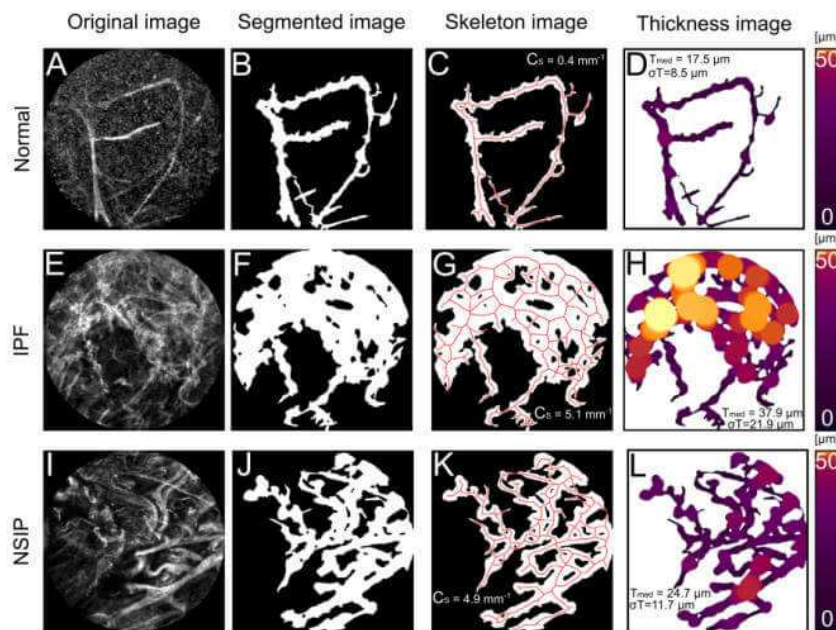


Fig 2. Three examples from every step of evaluation workflow. A-D) represent normal alveoli elastin structure with $T_{med} = 17.5 \mu m$, $\sigma_T = 8.5 \mu m$ and $C_s = 0.4 mm^{-1}$. E-H) represents IPF elastin structure with $T_{med} = 37.8 \mu m$, $\sigma_T = 21.9 \mu m$ and $C_s = 5.1 mm^{-1}$. I-L) represents NSIP structure with $T_{med} = 24.7 \mu m$, $\sigma_T = 11.7$ and $C_s = 4.9 mm^{-1}$.

<https://doi.org/10.1371/journal.pone.0232847.g002>

work presents a fully automatic workflow and demonstrated that the evaluation of elastin structure from pCLE snapshots can distinguish significant differences in elastin thickness and tissue connectivity between normal and DPLD alveoli. When evaluating the structural connectivity, median thickness and standard deviation of thickness COP, HP, NSIP and IPF showed

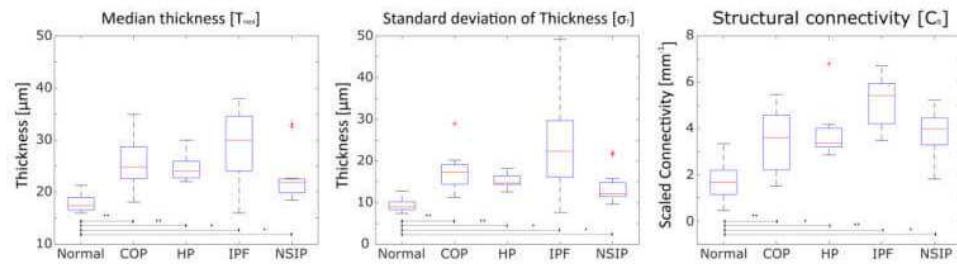


Fig 3. Value distributions of DPLD and normal structure evaluations for structural connectivity and thickness statistics. Box-and-whisker plots displaying value ranges for T_{med} , σ_T and C_s . Red line specifies group median. Bottom and top edges indicate the 25th and 75th percentiles, respectively and whiskers covers $\pm 2.698\sigma$. *: p-value < 0.05, **: p-value < 0.01.

<https://doi.org/10.1371/journal.pone.0232847.g003>

Table 1. Calculated median values for all measurement groups and difference between DPLDs and normal.

	$T_{\text{med-avg}}[\mu\text{m}]$	$\sigma_{T\text{-avg}}[\mu\text{m}]$	$C_{\text{s-avg}}[\text{mm}^{-1}]$	$\Delta T_{\text{med-avg}}[\mu\text{m}]$	$\Delta\sigma_{T\text{-avg}}[\mu\text{m}]$	$\Delta C_{\text{s-avg}}[\text{mm}^{-1}]$
Normal	17.4	8.9	1.66	N/A	N/A	N/A
COP	24.8	17.2	3.61	7.4 ($p = 6.1 \cdot 10^{-3}$)	8.3 ($p = 5.4 \cdot 10^{-3}$)	1.95 ($p = 9.3 \cdot 10^{-3}$)
HP	24.0	14.7	3.36	6.6 ($p = 3.7 \cdot 10^{-3}$)	5.8 ($p = 7.5 \cdot 10^{-3}$)	1.70 ($p = 0.013$)
IPF	30.0	22.3	5.42	12.6 ($p = 0.016$)	13.4 ($p = 0.014$)	3.76 ($p = 0.3 \cdot 10^{-3}$)
NSIP	21.8	12.1	3.78	4.3 ($p = 0.015$)	3.2 ($p = 0.019$)	2.12 ($p = 0.013$)

<https://doi.org/10.1371/journal.pone.0232847.t001>

significant differences in all three values compared to normal elastin structure. This suggests that the presented method for quantifying elastin of the alveoli can differentiate normal from diseased structures and can support fully automatic assistance in diagnosis of DPLD. Furthermore, since the method offers multiple parameters for differentiating between normal and pathological groups, more complex methods could potentially be developed for a holistic characterization.

In the presented study we opted for the conservative [28] Bonferroni p-value correction due to a small patient sample size. Since the scope of this study was to show that the presented methods can be of interest as a support tool when looking for DPLDs, we left further validation to future studies with larger sample sizes.

The presented method aims to quantify features that have previously been reported to change due to different DPLDs, such as increase/decrease of elastic fibres, disorganization of elastic network and enlarged axial elastic fibre bundle diameter [14–17]. Similar elastin thickness values were found here as in other work [29], albeit with a higher variability. This is to be expected considering that the presented method takes all of the structure in the FOV into consideration instead of only manually selected parts. To date, we know of no other quantitative analyses for the intricacies of a structure such as the presented structural connectivity value. Other observed structural changes [30] such as alveolar mouth size and increase of fluorescent were not taken into consideration in the presented methods.

Previous studies have focused on expert observer evaluation [14] or manual post processing methods [30,31] when comparing different elastin of the alveoli. The presented method instead offers quantitative values where the whole structure inside the FOV can be evaluated. Using the presented method when evaluating local thickness for example, offers an average of 2734 ± 1278 measurement points per patient which greatly reduces variability from outliers compared to manual thickness estimates.

A machine learning approach was used for the pixel classification to fully automate the segmentation step of the workflow, based on 21 snapshots from all patient measurements. Despite the small number, the segmentation algorithm succeeded in separating structures in noisy snapshots (Fig 2A and 2B) while still ignoring background structures (Fig 2I and 2J). Since DPLD has shown to decrease elastin's autofluorescence [13,32] it is of high interest to ensure that structures can be extracted even in low SNR snapshots. With the whole workflow running automatically, the opportunity emerges for quantitative assistance in real time during bronchoscopy examination. The presented method could be called upon in real time as a pulmonologist moves the pCLE probe through the lung and identifies a region of interest. The generated quantitative values can then be used to support the diagnosis of DPLD. Additionally, the suggested guiding capabilities of pCLE during cryobiopsy [33] can also benefit from the presented method's ability to highlight DPLD-structures by offering further objective validation before sampling.

Since the algorithm used for segmentation is open source, its functions can easily be called from other script languages. As more data is collected, the training model's segmentation capabilities can certainly be improved but also allows for the use of more complex methods. With deep learning approaches for example, structures could furthermore be fully automatically

selected, segmented [34] before analysis with the presented method. This would further the methods real-time capability and offer attending physicians suggestions of interesting ROI rather than confirmation.

There are some limitations in this study. The primary factors are the absence of a histological comparison to pCLE snapshots from the same regions in the lungs resulting in some uncertainty as to whether pCLE can offer 'optical biopsy'. Although the automatic segmentation's performance was satisfactory on most snapshots a larger measurement set is required to assess its capabilities on different DPLDs and still unseen descriptors by the machine learning algorithm.

Given that the snapshots are taken from a very small fraction of the whole lung this could lead to a poor morphological consistency of the evaluation method [16]. However, this is mitigated already by the use of a guiding tool such as HRCT to select representative areas of diseased tissue. Variability can also be decreased by utilizing average parameter values generated from multiple snapshots of different representative areas for every patient. Since pCLE is an in-vivo imaging technique complementing bronchoscopy, it does not suffer the same increase of risk associated with invasive techniques such as biopsy and could be used to examine multiple sections. So far, procedures performed in multiple studies have shown no severe side effects other than minor bleeding in 3 out of 42 patients [13,30] making it ideal for longitudinal studies.

As the presented method evaluates 3D structures on 2D images, unattached structures such as macrophages in the alveolar space could potentially overlap and appear to be part of the structure of interest. Furthermore, the workflow relies on the operating pulmonologist to ensure a proper orientation of the probe relative to the area of interest. The first problem was partly mitigated in this study by training the machine learning method to distinguish background structures from structures of interest, but more data would likely be required to test the model's generality. Future studies can further incorporate macrophages as a third segmentation class to expand on the analysis potential of the method. Consideration can also be taken by the performing pulmonologists if structures are overlapping or probe orientation needs adjustment when selecting snapshot. Validation cohorts would be required to confirm the clinical relevance of this method. In this initial study we have focused on the distinction between normal and DPLD alveoli due to the small sample size. A next step would be to establish respective value ranges for different types of pathologies aiming to further assess the presented methods' diagnostic potential.

Conclusion

In this study we presented a method for the quantitative evaluation of alveolar elastin structure using pCLE images. We demonstrated that quantifying structural properties of the alveoli elastin, such as thickness and connectivity, allows for the differentiation of DPLD and normal lung tissue. We furthermore presented a framework for a fully automated workflow that can be easily implemented into pCLE examinations. This can offer further assistance by providing quantitative values to pulmonologists for the diagnosis of DPLDs.

Supporting information

S1 Data.
(ZIP)

Author Contributions

Conceptualization: David Bondesson, Moritz J. Schneider, Edith Silbernagel, Jürgen Behr, Frank Reichenberger, Julien Dinkel.

Data curation: Edith Silbernagel, Frank Reichenberger, Julien Dinkel.

Formal analysis: David Bondesson.

Funding acquisition: Jürgen Behr, Julien Dinkel.

Investigation: Edith Silbernagel, Frank Reichenberger, Julien Dinkel.

Methodology: David Bondesson, Moritz J. Schneider, Jürgen Behr, Julien Dinkel.

Project administration: David Bondesson, Moritz J. Schneider, Jürgen Behr, Julien Dinkel.

Resources: Edith Silbernagel, Jürgen Behr, Frank Reichenberger, Julien Dinkel.

Software: David Bondesson.

Supervision: Moritz J. Schneider, Jürgen Behr, Julien Dinkel.

Validation: David Bondesson, Moritz J. Schneider, Edith Silbernagel, Frank Reichenberger.

Visualization: David Bondesson, Moritz J. Schneider.

Writing – original draft: David Bondesson.

Writing – review & editing: David Bondesson, Moritz J. Schneider, Edith Silbernagel, Jürgen Behr, Frank Reichenberger, Julien Dinkel.

References

1. Flaherty KR, King TE, Raghu G, Lynch JP, Colby TV, Travis WD, et al. Idiopathic Interstitial Pneumonia. *Am J Respir Crit Care Med*. 2004 Oct 15; 170(8):904–10. <https://doi.org/10.1164/rccm.200402-147OC> PMID: 15256390
2. Raghu G, Collard HR, Egan JJ, Martinez FJ, Behr J, Brown KK, et al. An Official ATS/ERS/JRS/ALAT Statement: Idiopathic Pulmonary Fibrosis: Evidence-based Guidelines for Diagnosis and Management. *Am J Respir Crit Care Med*. 2011 Mar 15; 183(6):788–824. <https://doi.org/10.1164/rccm.2009-040GL> PMID: 21471066
3. Doyle TJ, Hunninghake GM, Rosas IO. Subclinical Interstitial Lung Disease. *Am J Respir Crit Care Med*. 2012 Jun 1; 185(11):1147–53. <https://doi.org/10.1164/rccm.201108-1420PP> PMID: 22366047
4. Hodnett PA, Naidich DP. Fibrosing Interstitial Lung Disease. A Practical High-Resolution Computed Tomography-based Approach to Diagnosis and Management and a Review of the Literature. *Am J Respir Crit Care Med*. 2013 May 14; 188(2):141–9. <https://doi.org/10.1164/rccm.201208-1544CI> PMID: 23672718
5. Lynch DA, Sverzellati N, Travis WD, Brown KK, Colby TV, Galvin JR, et al. Diagnostic criteria for idiopathic pulmonary fibrosis: a Fleischner Society White Paper. *Lancet Respir Med*. 2018 Feb 1; 6(2):138–53. [https://doi.org/10.1016/S2213-2600\(17\)30433-2](https://doi.org/10.1016/S2213-2600(17)30433-2) PMID: 29154106
6. Martinez FJ, Chisholm A, Collard HR, Flaherty KR, Myers J, Raghu G, et al. The diagnosis of idiopathic pulmonary fibrosis: current and future approaches. *Lancet Respir Med*. 2017 Jan 1; 5(1):61–71. [https://doi.org/10.1016/S2213-2600\(16\)30325-3](https://doi.org/10.1016/S2213-2600(16)30325-3) PMID: 27932290
7. Hetzel J, Maldonado F, Ravaglia C, Wells AU, Colby TV, Tomassetti S, et al. Transbronchial Cryobiopsies for the Diagnosis of Diffuse Parenchymal Lung Diseases: Expert Statement from the Cryobiopsy Working Group on Safety and Utility and a Call for Standardization of the Procedure. *Respiration*. 2018; 95(3):188–200. <https://doi.org/10.1159/000484055> PMID: 29316560
8. Thiberville L, Moreno-Swirc S, Vercauteren T, Peltier E, Cavé C, Bourg Heckly G. In Vivo Imaging of the Bronchial Wall Microstructure Using Fibered Confocal Fluorescence Microscopy. *Am J Respir Crit Care Med*. 2007 Jan 1; 175(1):22–31. <https://doi.org/10.1164/rccm.200605-684OC> PMID: 17023733
9. Goualher GL, Perchant A, Genet M, Cavé C, Viellerobe B, Berier F, et al. Towards Optical Biopsies with an Integrated Fibered Confocal Fluorescence Microscope. In: *Medical Image Computing and Computer-Assisted Intervention—MICCAI 2004* [Internet]. Springer, Berlin, Heidelberg; 2004 [cited 2019 Mar 5]. p. 761–8. https://link.springer.com/chapter/10.1007/978-3-540-30136-3_93
10. Lee P, Brokx HAP, Postmus PE, Sutedja TG. Dual digital video-autofluorescence imaging for detection of pre-neoplastic lesions. *Lung Cancer Amst Neth*. 2007 Oct; 58(1):44–9.

11. Ikeda N, Hayashi A, Iwasaki K, Honda H, Tsuboi M, Usuda J, et al. Comprehensive diagnostic bronchoscopy of central type early stage lung cancer. *Lung Cancer*. 2007 Jun 1; 56(3):295–302. <https://doi.org/10.1016/j.lungcan.2007.01.009> PMID: 17291623
12. Thiberville L, Salaün M. Bronchoscopic Advances: On the Way to the Cells. *Respiration*. 2010; 79(6):441–9. <https://doi.org/10.1159/000313495> PMID: 20431326
13. Newton RC, Kemp SV, Yang G-Z, Elson DS, Darzi A, Shah PL. Imaging parenchymal lung diseases with confocal endomicroscopy. *Respir Med*. 2012 Jan; 106(1):127–37. <https://doi.org/10.1016/j.rmed.2011.09.009> PMID: 22000588
14. Filner JJ, Bonura EJ, Lau ST, Abounasr KK, Naidich D, Morice RC, et al. Bronchoscopic Fibred Confocal Fluorescence Microscopy Image Characteristics and Pathologic Correlations. *J Bronchol Interv Pulmonol*. 2011 Jan; 18(1):23.
15. Yick CY, von der Thüsen JH, Bel EH, Sterk PJ, Kunst PW. In vivo imaging of the airway wall in asthma: fibred confocal fluorescence microscopy in relation to histology and lung function. *Respir Res*. 2011; 12(1):85. <https://doi.org/10.1186/1465-9921-12-85> PMID: 21699692
16. Yserbyt J, Dooms C, Decramer M, Verleden GM. Probe-based confocal laser endomicroscopy of the respiratory tract: A data consistency analysis. *Respir Med*. 2013 Aug 1; 107(8):1234–40. <https://doi.org/10.1016/j.rmed.2013.04.018> PMID: 23706778
17. Meng P, Tan GL, Low SY, Takan A, Ng YL, Anantham D. Fibred confocal fluorescence microscopy in the diagnosis of interstitial lung diseases. *J Thorac Dis*. 2016 Dec 28; 8(12):3505–3514.
18. Zadrozny B, Elkan C. Obtaining Calibrated Probability Estimates from Decision Trees and Naive Bayesian Classifiers. In: Proceedings of the Eighteenth International Conference on Machine Learning [Internet]. San Francisco, CA, USA: Morgan Kaufmann Publishers Inc.; 2001 [cited 2019 Jul 1]. p. 609–616. (ICML '01). <http://dl.acm.org/citation.cfm?id=645530.655658>
19. Arganda-Carreras I, Kaynig V, Rueden C, Eliceiri KW, Schindelin J, Cardona A, et al. Trainable Weka Segmentation: a machine learning tool for microscopy pixel classification. *Bioinformatics*. 2017 Aug 1; 33(15):2424–6. <https://doi.org/10.1093/bioinformatics/btx180> PMID: 28369169
20. Schindelin J, Arganda-Carreras I, Frise E, Kaynig V, Longair M, Pietzsch T, et al. Fiji: an open-source platform for biological-image analysis. *Nat Methods*. 2012 Jul; 9(7):676–82. <https://doi.org/10.1038/nmeth.2019> PMID: 22743772
21. Chawla NV. Data Mining for Imbalanced Datasets: An Overview. In: Maimon O, Rokach L, editors. *Data Mining and Knowledge Discovery Handbook* [Internet]. Boston, MA: Springer US; 2010 [cited 2019 Sep 20]. p. 875–86. https://doi.org/10.1007/978-0-387-09823-4_45
22. Peng Hanchuan, Long Fuhui, Ding C. Feature selection based on mutual information criteria of max-dependency, max-relevance, and min-redundancy. *IEEE Trans Pattern Anal Mach Intell*. 2005 Aug; 27(8):1226–38. <https://doi.org/10.1109/TPAMI.2005.159> PMID: 16119262
23. Pratt WK. *Digital Image Processing: PIKS Scientific inside* [Internet]. 4th Edition. New York: John Wiley & Sons, INC; 2007 [cited 2019 Jun 18]. 623 p. https://www.academia.edu/30586970/Digital_Image_Processing_4th_Edition_-_William_K_Pratt
24. Friedman JH, Bentley JL, Finkel RA. An Algorithm for Finding Best Matches in Logarithmic Expected Time. *ACM Trans Math Softw*. 1977 Sep; 3(3):209–226.
25. Wilcoxon F. Individual Comparisons by Ranking Methods. *Biom Bull*. 1945; 1(6):80–3.
26. Bland JM, Altman DG. Multiple significance tests: the Bonferroni method. *BMJ*. 1995 Jan 21; 310(6973):170. <https://doi.org/10.1136/bmj.310.6973.170> PMID: 7833759
27. Silbernagel E, Bondesson D, Behr J, Dinkel J, Reichenberger F. Taking Another View on Lung Fibrosis. *Am J Respir Crit Care Med*. 2018 Feb 2; 197(7):947–8. <https://doi.org/10.1164/rccm.201708-1883IM> PMID: 29394081
28. Perneger TV. What's wrong with Bonferroni adjustments. *BMJ*. 1998 Apr 18; 316(7139):1236–8. <https://doi.org/10.1136/bmj.316.7139.1236> PMID: 9553006
29. Salaun M, Dominique S, Rousset F, Genevois A, Jounieaux V, Zalcmán G, et al. In vivo probe-based confocal laser endomicroscopy in chronic diffuse parenchymal lung diseases. *Eur Respir J*. 2012 Sep 1; 40(Suppl 56):P3603.
30. Salaun M, Guisier F, Dominique S, Genevois A, Jounieaux V, Bergot E, et al. In vivo probe-based confocal laser endomicroscopy in chronic interstitial lung diseases: Specific descriptors and correlation with chest CT. *Respirology*. 2019 Aug 1; 24(8):783–91. <https://doi.org/10.1111/resp.13507> PMID: 30811085
31. Yserbyt J, Dooms C, Decramer M, Verleden GM. Acute lung allograft rejection: Diagnostic role of probe-based confocal laser endomicroscopy of the respiratory tract. *J Heart Lung Transplant*. 2014 May 1; 33(5):492–8. <https://doi.org/10.1016/j.healun.2014.01.857> PMID: 24656287

32. Peng M, Liang TG, Anantham D. Probe-Based Confocal Laser Endomicroscopy of the Lungs. *J Pulm Respir Med* [Internet]. 2016 [cited 2019 Jul 2]; 6(5). Available from: <https://www.omicsonline.org/open-access/probebased-confocal-laser-endomicroscopy-of-the-lungs-2161-105X-1000373.php?aid=81460>
33. Hariharan B, Arbeláez P, Girshick R, Malik J. Simultaneous Detection and Segmentation. In: Fleet D, Pajdla T, Schiele B, Tuytelaars T, editors. *Computer Vision—ECCV 2014*. Springer International Publishing; 2014. p. 297–312. (Lecture Notes in Computer Science).
34. Wijmans L, Bonta PI, Rocha-Pinto R, de Bruin DM, Brinkman P, Jonkers RE, et al. Confocal Laser Endomicroscopy as a Guidance Tool for Transbronchial Lung Cryobiopsies in Interstitial Lung Disorder. *Respiration*. 2019; 97(3):259–63. <https://doi.org/10.1159/000493271> PMID: 30428462

3.2 Bondesson D, Gaass T, Dinkel J, Kiefer B. Non-contrast-enhanced perfusion and ventilation assessment of the human lung by means of wavelet decomposition in proton MRI. *Proc Intl Soc Mag Reson Med* 2016; 24:1934. [https:// doi-org.emediennub.uni-muenchen.de/10.1002/mrm.27803](https://doi-org.emediennub.uni-muenchen.de/10.1002/mrm.27803)

Nonuniform Fourier-decomposition MRI for ventilation- and perfusion-weighted imaging of the lung

David Bondesson^{1,2} | Moritz J. Schneider^{1,2} | Thomas Gaass³ | Bernd Kühn⁴ |
Grzegorz Bauman^{5,6} | Olaf Dietrich¹ | Julien Dinkel^{1,2}

¹Department of Radiology, University Hospital, LMU Munich, Munich, Germany

²Comprehensive Pneumology Center (CPC-M), German Center for Lung Research (DZL), Munich, Germany

³Siemens Healthcare Pty Ltd, Bowen Hills, Australia

⁴Siemens Healthcare GmbH, Erlangen, Germany

⁵Division of Radiological Physics, Department of Radiology, University of Basel Hospital, Basel, Switzerland

⁶Department of Biomedical Engineering, University of Basel, Basel, Switzerland

Correspondence

David Bondesson, Marchioninstr. 15,
Munich, Bavaria, Germany 81377.
Email: david.bondesson@med.uni-
muenchen.de

Funding information

The authors acknowledge partial funding by the German Center for Lung Research (DZL), but received no specific grant for this research from any funding agency in the public, commercial or not-for-profit sector.

Purpose: To improve the robustness of pulmonary ventilation- and perfusion-weighted imaging with Fourier decomposition (FD) MRI in the presence of respiratory and cardiac frequency variations by replacing the standard fast Fourier transform with the more general nonuniform Fourier transform.

Theory and Methods: Dynamic coronal single-slice MRI of the thorax was performed in 11 patients and 5 healthy volunteers on a 1.5T whole-body scanner using a 2D ultra-fast balanced steady-state free-precession sequence with temporal resolutions of 4-9 images/s. For the proposed nonuniform Fourier-decomposition (NUFD) approach, the original signal with variable physiological frequencies that was acquired with constant sampling rate was retrospectively transformed into a signal with (ventilation or perfusion) frequency-adapted sampling rate. For that purpose, frequency tracking was performed with the synchro-squeezed wavelet transform. Ventilation- and perfusion-weighted NUFD amplitude and signal delay maps were generated and quantitatively compared with regularly sampled FD maps based on their signal-to-noise ratio (SNR).

Results: Volunteers and patients showed statistically significant increases of SNR in frequency-adapted NUFD results compared to regularly sampled FD results. For ventilation data, the mean SNR increased by $43.4\% \pm 25.3\%$ and $24.4\% \pm 31.9\%$ in volunteers and patients, respectively; for perfusion data, SNR increased by $93.0\% \pm 36.1\%$ and $75.6\% \pm 62.8\%$. Two patients showed perfusion signal in pulmonary areas with NUFD that could not be imaged with FD.

Olaf Dietrich and Julien Dinkel contributed equally to this work.

This is an open access article under the terms of the Creative Commons Attribution-NonCommercial License, which permits use, distribution and reproduction in any medium, provided the original work is properly cited and is not used for commercial purposes.

© 2019 The Authors. *Magnetic Resonance in Medicine* published by Wiley Periodicals, Inc. on behalf of International Society for Magnetic Resonance in Medicine

Conclusion: This study demonstrates that using nonuniform Fourier transform in combination with frequency tracking can significantly increase SNR and reduce frequency overlaps by collecting the signal intensity onto single frequency bins.

KEYWORDS

Fourier decomposition, lung, nonuniform Fourier transform, pulmonary MRI

1 | INTRODUCTION

Pulmonary Fourier-decomposition (FD) MRI is a noninvasive free-breathing imaging method for extracting functional information about ventilation and perfusion in the lung.¹ FD MRI works on a registered series of dynamically acquired MR images of the lung, in which periodic signal changes associated with perfusion and ventilation can be spectrally separated and subsequently analyzed. Both signal variations are correlated with proton density variations, which are caused by changes in capillary blood filling (together with intravoxel dephasing effects) or changes in alveoli density, respectively.²⁻⁴

Several studies have shown the FD method to be a viable tool for spotting local pulmonary pathologies^{5,6} without requirement of contrast-agent administration (neither intravenous agents for perfusion nor gaseous agents for ventilation assessment) or the health risks of radiation-based methods (as, e.g., CT or single photon emission CT). In addition to mapping the spectral amplitude, it has also been suggested that the phase information obtained by FD MRI could potentially be used for estimating the signal arrival time. The phase difference (between 2 voxels) of a single spectral frequency component is proportional to the temporal shift of the signals. Consequently, the signal arrival time (i.e., the “signal delay”) can be mapped by evaluating the phase difference compared to a starting point. Thus, localized delays of spatial signal propagation caused by pathologies such as cystic fibrosis, chronic obstructive pulmonary disease, chronic thromboembolic pulmonary hypertension (CTEPH), asthma, or idiopathic pulmonary fibrosis^{7,8} could be displayed.

However, inevitable random variations of respiratory or cardiac frequencies during free-breathing pulmonary measurements can be reason for artificial signal loss when using the established FD MRI approach. Related methods that have been proposed to overcome this problem require complex multiple-step post-processing including peak finding, exact phase estimation and data resorting of k-space⁹ or image-space data¹⁰ to use all of the measured signal variations as well as recalibrate the signal contribution to a single frequency.

The purpose of this study was to return to the conceptual simplicity of the initially proposed FD method and to improve its robustness (quantified in terms of signal-to-noise ratio [SNR] maps) in the presence of frequency variations by replacing the well-known fast Fourier transform with the

more general nonuniform fast Fourier transform (NUFFT). This nonuniform Fourier-decomposition (NUFD) approach requires transforming the original, evenly sampled signal with variable frequency into a signal with constant frequency that is sampled at varying rate.

2 | THEORY

In almost all real-time ventilation and perfusion measurements, signal frequencies vary nonlinearly over time. When calculating the Fourier transform, this will not only spread the resulting intensity over multiple frequency bins, but also cause phase errors if spectral content overlaps. In the following sections, an approach is described to correct for such frequency variations.

2.1 | Signal sampling

In the following, we consider an oscillating signal $S(t)$ with varying frequency $f(t)$ and assume that $S(t)$ is sampled at equidistant sampling times $t_n = n\Delta t$ with the constant sampling interval Δt . If the signal frequency $f(t)$ is varying, then the numbers of sample points t_n per signal cycle will change correspondingly (cf. Figure 1A). However, by transforming the original sampling times t_n (together with the sampled signal intensities) to “virtual,” nonequidistant sampling times \tilde{t}_n , the same sampled intensities appear as the time course of a virtual single-frequency signal $\tilde{S}(\tilde{t})$ (cf. Figure 1B). Thus, a uniformly sampled signal with variable frequency can be transformed into a nonuniformly sampled signal with constant frequency.

The calculation of the appropriate virtual, nonequidistant sampling times \tilde{t}_n can be based on the instantaneous frequency $f(t)$ of the signal, which can be determined by appropriate frequency-tracking techniques as described below. To obtain identical virtual cycle durations of $\tilde{S}(\tilde{t})$, the n -th sampling intervals $\Delta\tilde{t}_n$ must be modified proportional to the tracked frequency

$$\Delta\tilde{t}_n = \Delta t \frac{f(t_n)}{f_{\text{mean}}} \quad (1)$$

resulting in the new sampling times

$$\tilde{t}_n = \sum_{k=1}^n \Delta\tilde{t}_k = \frac{\Delta t}{f_{\text{mean}}} \sum_{k=1}^n f(t_k) \quad (2)$$

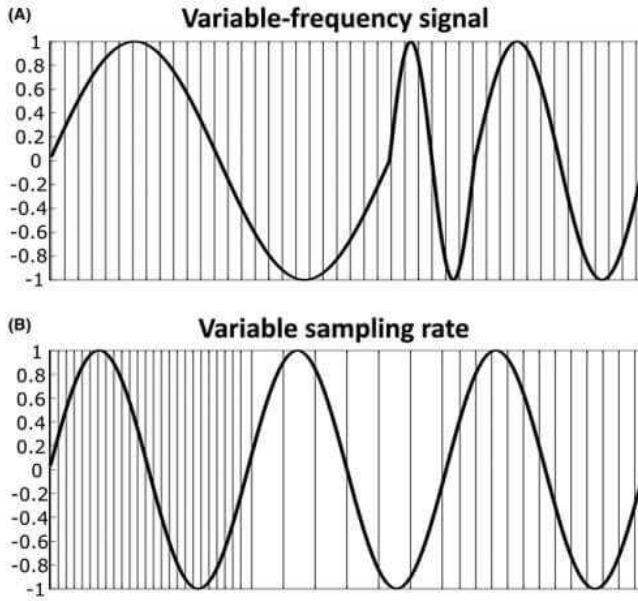


FIGURE 1 Constant and frequency-adapted sampling rate. A, Variable-frequency signal with constant sampling rate; the frequency varies every signal cycle. B, Constant-frequency signal with variable sampling rates; the same signal as above has been transformed into a constant-frequency signal by appropriately modifying the sampling rates

The scaling factor f_{mean} is to be chosen such that the total sampling duration remains the same, i.e. $\bar{t}_N - \bar{t}_1 = t_N - t_1$. Assuming $\bar{t}_1 = t_1 = 0$, this is achieved by setting f_{mean} to the mean value of the tracked frequency:

$$f_{\text{mean}} = \frac{1}{N} \sum_{k=1}^N f(t_k). \quad (3)$$

2.2 | NUFFT

Based on the new (virtual) sampling times \bar{t}_n the selected frequency component F_k (containing, e.g., the ventilation or the perfusion component of a pulmonary measurement) of the signal $\tilde{S}(\bar{t})$ can be quantified by Fourier analysis. However, because the sampling times \bar{t}_n are not equidistant, this cannot be done using standard FFT algorithms; instead, a type-1 NUFFT is required to calculate the (equidistant) frequency spectrum of a signal defined at nonequidistant time points.⁹ The type-1 discrete nonuniform Fourier transform is defined as

$$F_k = \text{NUFFT}(\tilde{S}(\bar{t}_n)) = \sum_{n=1}^N \tilde{S}(\bar{t}_n) \exp(-2\pi i k \bar{t}_n / (\bar{t}_N - \bar{t}_1)) \Delta t$$

This looks similar to a regular discrete Fourier transform with the modification that the sampling times \bar{t}_n are not evenly spaced.

3 | METHODS

3.1 | Image acquisition

Five healthy volunteers (24–28 years old; 2 female and 3 male) and 11 patients (5 with suspicion of CTEPH, 4 with suspicion of idiopathic pulmonary arterial hypertension (PAH) and 2 with suspicion of idiopathic pulmonary fibrosis, 31–84 years old; 5 female and 6 male) underwent non-contrast-enhanced MRI under free-breathing conditions. None of the healthy volunteers were smokers. Participants were measured as preparation and part of a study (registration number NCT02791282) and written informed consent was obtained from all subjects. Patients with pulmonary hypertension were referred to the study by means of the pneumology department with no other exclusion criteria than being able to undergo 25 min of measurement; thus, only the most severe cases were excluded. MRI was performed on a 1.5T whole-body scanner (Siemens Magnetom Aera, Siemens Healthineers, Erlangen, Germany) with an 18-channel body array coil and 16 elements of a spine array coil. Functional MRI data were acquired in supine position (head first) for a single coronal mid-lung slice per subject. Dynamic single-slice imaging was performed with a 2D ultra-fast balanced steady-state free-precession (uf-bSSFP) sequence,¹¹ optimized to distinguish signal variations in the lung parenchyma. The main pulse sequence parameters were as follows: field of view = $450 \times 450 \text{ mm}^2$, matrix = 96×96 voxels, slice thickness = 15 mm, repetition time = 1.03 ms, echo time = 0.36 ms,

flip angle: 24.5° for volunteers and $24.5\text{--}80^\circ$ for patients. For volunteers, the temporal resolution was 115 ms/image, the series consisted of 1024 images, resulting in total measurement times of 117 s. For the patients, the temporal resolution varied between 115 and 216 ms/image, the series consisted of 200 to 1024 images, resulting in total measurement times between 40 and 117 s.

One of the 5 healthy test subject measurements was repeated 6 times with changing amounts of frequency variability between them to investigate the stability of the compensation. The frequency variability was simply yielded by asking the test subject to change their ventilation rate more or less within each measurement. Due to respiratory sinus arrhythmia¹² increased necessity for frequency tracking in both perfusion and ventilation signal components was expected.

3.2 | Image processing workflow

A prototype software, fMRLung 4.5 (Siemens Digital Services, Princeton, NJ) was used to apply a nonrigid registration algorithm^{13,14} to the measured image series. The

reference image was chosen manually based on the mean value of the diaphragm signal in the apical–basal direction to yield mid-ventilation position.

All further image processing was performed with Matlab (The MathWorks, Natick, MA). The first 20 images were discarded due to transient signal behavior of the uf-bSSFP sequence. In every voxel, the DC signal was subtracted from the time signal to focus purely on the variations. A region of interest (ROI) was manually segmented (with function 'roipoly, Matlab version 2018a) along the pleural lines covering both pulmonary veins as well as parenchyma collecting both average perfusion and ventilation signal variations. Subject-specific bandpass filtering was applied to separate ventilation and perfusion components similar to the standard FD method. Additional high pass filtering was applied on the ventilation-weighted signal to remove frequencies below 0.07 Hz (corresponding to signal periods longer than 14 s), which were considered baseline drift being substantially slower than realistic breathing (Figure 2A).

Frequency tracking of the resulting signal-time course was performed with the synchro-squeezed wavelet transform (SWT) method (function "wsst", Matlab version 2018a),¹⁵

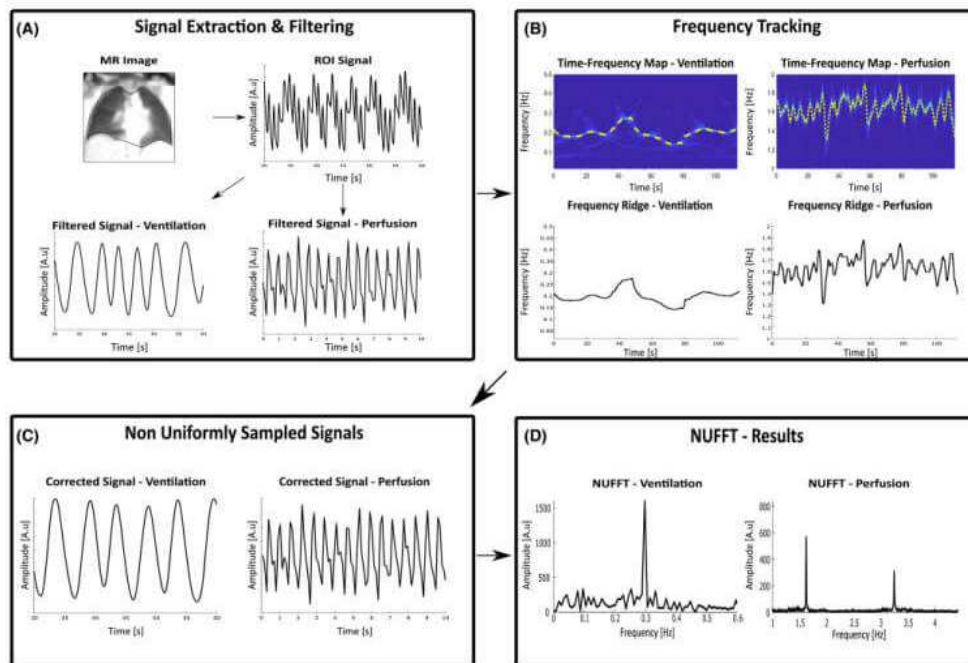


FIGURE 2 Workflow of NUFFT MRI image processing. A, Extraction of ventilation and perfusion signal from large ROI by band-pass filtering. B, Resulting time-frequency map from SWT with tracked frequencies from ridge detection. C, Ventilation and perfusion signals displayed with recalculated sampling points (frequency variations are reduced in comparison to A). D, Resulting NUFFT spectra from the curves in C, showing that intensity has indeed been collected onto a single frequency bin for both ventilation and perfusion

which resulted in a 2D frequencies-over-time spectrum (time-frequency map in Figure 2B, top). For SWT, the analytical Morlet wavelet was selected as a mother wavelet over bump wavelet, due to its narrower variance in time dimension. To track the frequency of interest, a method called ridge detection can be used; e.g., the function “wsstridge” in Matlab.¹⁶ Ridge detection (Figure 2B, bottom) follows the frequency of the maximum intensity signal component in the SWT spectrum by means of a penalized forward backward greedy algorithm. The penalty parameter limits large frequency jumps and was set to 0.3.

New “virtual” sampling times were then calculated with Equation 2, as described above (Figure 2C). Then, NUFFT was performed on the averaged lung ROI data, yielding 2 frequency spectra (1 for ventilation, 1 for perfusion), in which the relevant frequency bins for ventilation f_{vent} or perfusion f_{perf} could be determined (Figure 2D). The NUFFT was implemented^b in Matlab with a Gaussian gridding based method,^{17,18} which has shown to yield better reconstruction performance for NUFFT estimations than methods combining other types of interpolation with standard FFT.¹⁹

Finally, ventilation- and perfusion-weighted maps were generated applying the NUFFT analysis (with the new sampling times determined above) for every lung voxel, similar as with the FD method. Amplitude maps were then calculated from the frequency spectra with the ventilation and perfusion frequencies f_{vent} and f_{perf} extracted from the averaged ROI time signal.

Using the complex phase of the spectral frequency bin of every voxel (after applying a 2D phase unwrapping algorithm,²⁰ another map termed “(signal) delay map” was generated showing the delay of the signal relative to a reference voxel. The actual time delay t_{delay} was calculated for each voxel as

$$t_{delay} = \frac{\phi_0 - \phi}{2\pi} T = \frac{\phi_0 - \phi}{2\pi f} \quad (5)$$

where ϕ is the phase angle, ϕ_0 is the phase of a reference voxel (with the highest phase value, i.e., lowest time delay in the analyzed ROI), and T is the cycle period, i.e., the inverse frequency $T = \frac{1}{f}$ of the ventilation or perfusion frequencies f_{vent} and f_{perf} .

For comparison, FD maps (with amplitude data and phase-based temporal delay data) were produced for all measurements.

3.3 | Image evaluation

A standard method for SNR calculation of Fourier transforms is to compare the amplitude of the signal frequency

bin to the power of the noise frequency bins.²¹ In the present study, SNR maps were calculated by dividing the signal of the ventilation and perfusion maps by the standard deviation of the noise bins of each lung voxel. The SNR maps were manually and separately segmented for both perfusion and ventilation evaluation. The perfusion ROI excluded the lower left lung where the heart moved into the section; the ventilation ROI excluded the large pulmonary vessels. To quantify and compare these SNR maps, the average SNR (mean value) within the ROI was then calculated. The percentage difference between SNR for the NUFD and FD method was then calculated. Statistical evaluation was lastly performed with 1-sample t-tests (2-tailed) on percentage change of SNR, for patient and volunteer measurements, respectively. Differences were considered to be statistically significant if P -values were less than 0.05.

4 | RESULTS

4.1 | SNR evaluation

Comparing NUFD to FD evaluation, a statistically significant increase of average ventilation and perfusion SNRs of healthy volunteers was found (including all measurements from the variable frequency test). Ventilation SNRs increased by $43.4\% \pm 25.3\%$ ($P < 0.001$) and perfusion SNRs by $93.0\% \pm 36.1\%$ ($P < 0.001$). The average increase of all eleven patients' ventilation and perfusion SNRs from NUFD compared to FD was also statistically significant with $24.4\% \pm 31.9\%$ ($P = 0.03$) and $75.6\% \pm 62.8\%$ ($P = 0.003$), respectively. All results are summarized in the Table 1.

Figure 3 displays an example of the resulting frequency spectra from the averaged ROI signal of a typical volunteer measurement, comparing the NUFD and FD approach. The spread-out frequency components of the FD approach have been collected and are clearly not overlapping in the NUFD results. In addition, both NUFD ventilation and perfusion have gained a clear increase of amplitude.

Figure 4 shows examples of SNR maps from the same measurement. Both ventilation and perfusion maps display substantially higher SNRs with the NUFD approach compared to the FD evaluation.

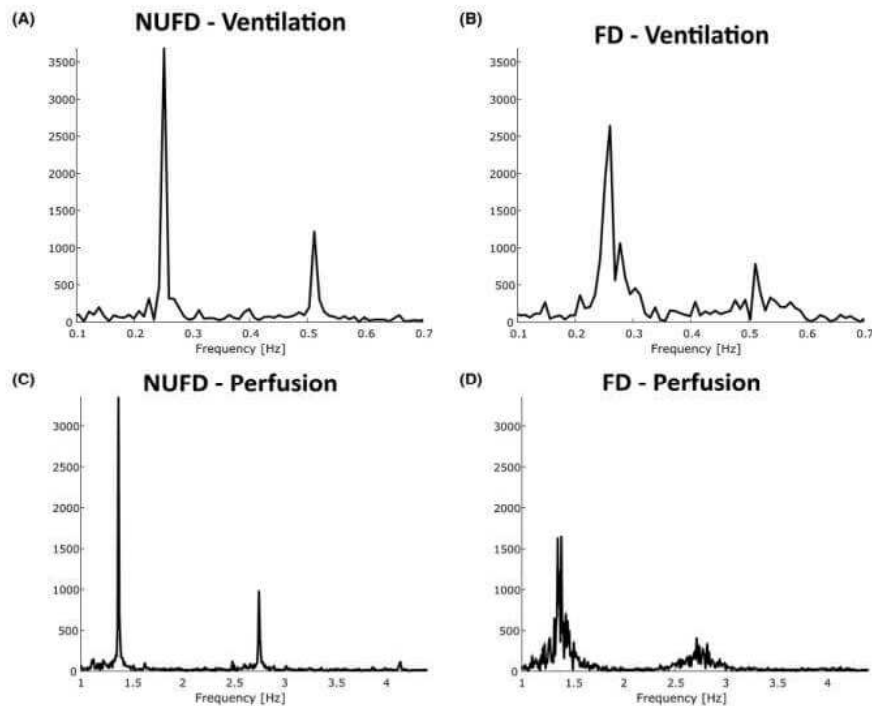
4.2 | Influence of frequency variability and volunteer data

Two of the resulting NUFD and FD maps from the repeated volunteer measurements with different ventilation frequency variability are presented in Figure 5. Improvements due to the NUFD approach were especially prominent in ventilation delay maps of measurement 2, in which the volunteer was asked to breathe very irregularly. Using the FD method

TABLE 1 SNR results for ventilation and perfusion measurements from FD and NUFD method displaying average and standard deviation SNR of volunteer and patient measurements

	SNR NUFD	SNR FD	SNR increase (absolute)	SNR increase (relative)	P-Value
Volunteer ventilation ($n=11$)	144.1 \pm 32.6	102.7 \pm 27.8	41.4 \pm 17.7	43.4% \pm 25.3%	2×10^{-5}
Volunteer perfusion ($n=11$)	52.3 \pm 11.6	27.8 \pm 6.8	24.5 \pm 8.3	93.0% \pm 36.1%	7×10^{-6}
Patients ventilation ($n=11$)	121.8 \pm 64.5	95.1 \pm 41.1	26.7 \pm 36.3	24.4% \pm 31.9%	3×10^{-2}
Patients perfusion ($n=11$)	18.5 \pm 13.5	11.2 \pm 7.5	7.3 \pm 7.9	75.6% \pm 62.8%	3×10^{-3}

Average and standard deviation increase in SNR (absolute and relative) between the 2 methods are also summarized with associated *P*-values.

**FIGURE 3** Frequency spectra from NUFD (A,C) and FD (B,D) MRI based on extracted and averaged ROI signal for ventilation (A,B) and perfusion (C,D) component

resulted in a different signal delay pattern in the ventilation case. Comparing the ventilation delay patterns between measurements 1 and 2, the NUFD map of measurement 2 was substantially more similar to measurement 1 than the FD maps. Generally, the perfusion delay maps illustrate consistently the propagation of the perfusion signal from the large central vessels to the pulmonary periphery.

In Table 2 below, a clearly improved average SNR is presented when comparing the NUFD and FD maps. However,

it should be noted that the SNR increase was not linearly correlated with frequency variability. In fact, the highest ventilation frequency variability yielded the smallest increase in the estimation of measurement 2.

The NUFD delays of perfusion (i.e., $t_{\text{delay,max}} - t_{\text{delay,min}}$ within an individual map) ranged from 70 to 185 ms for the different volunteers (mean value over all volunteers was 126 ± 42.5 ms); for ventilation, the NUFD delays ranged from 180 to 370 ms (mean value was 280 ± 68.9 ms).

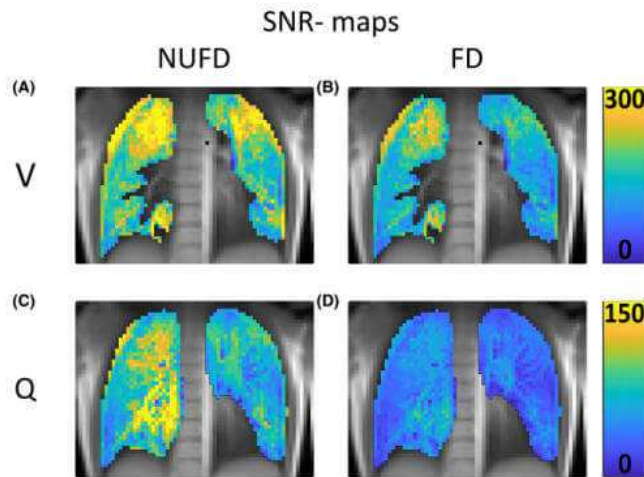


FIGURE 4 SNR maps generated from NUFD and regularly sampled FD spectra in a healthy volunteer. A,B, Ventilation (V) SNR maps displaying average SNRs of 195.3 and 144.2, respectively, corresponding to a +35.4% increase of SNR. C,D, Perfusion (Q) SNR maps displaying average SNRs of 80 and 39 corresponding to a +106% increase of SNR

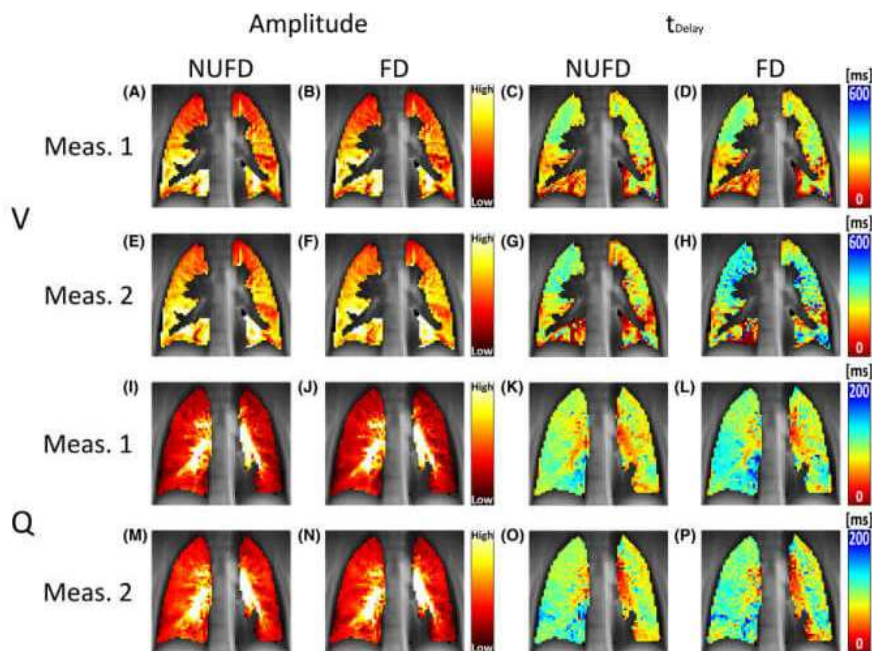


FIGURE 5 Influence of frequency variability. A-H, Ventilation-weighted (V) amplitude and signal delay maps from 2 measurements; the standard deviations of the ventilation frequencies were 0.01 Hz and 0.11 Hz, respectively. I-P, Perfusion-weighted (Q) amplitude and signal delay maps from 2 measurements; the standard deviations of cardiac frequencies were 0.04 Hz and 0.03 Hz, respectively

TABLE 2 Resulting average SNR from 6 measurements with varying frequency variability

	Ventilation						Perfusion					
	1	2	3	4	5	6	1	2	3	4	5	6
std(f) (Hz)	0.014	0.11	0.03	0.05	0.05	0.04	0.04	0.07	0.09	0.06	0.05	0.05
mean(f) (Hz)	0.12	0.20	0.15	0.20	0.14	0.14	0.95	1.04	0.96	1.04	0.96	0.99
mean(SNR _{FD})	96.6	99.7	82.4	72.4	82.4	91.9	35.1	21.0	27.1	21.7	32.4	27.1
mean(SNR _{NUFD})	144.8	103.3	111.8	127.9	111.2	130.2	66.0	47.6	43.8	52.9	43.5	48.9
increase (SNR)	48.2	3.5	29.4	55.5	28.8	38.3	30.9	26.6	16.8	31.2	11.1	21.8
increase (SNR) %	50%	4%	36%	77%	35%	42%	88%	127%	62%	144%	34%	81%

Table describes frequency variability std(f) (standard deviation of the tracked frequency) and mean frequency mean(f) for perfusion and ventilation signals with SNRs from FD and NUFD method as well as the absolute and relative SNR increase.

4.3 | Patient data

Two patients, 1 with suspicion of CTEPH and 1 with suspicion of PAH are presented in Figure 6. Both show large perfusion defects in the amplitude maps from both the FD and NUFD methods. However, when using the NUFD method, the SNR was increased in the perfusion maps for both measurements (from 11.5 to 19.6 in the CTEPH case, yielding 71% increase and from 7.2 to 10.7 in the PAH case, yielding 48% increase). This ensured that weaker blood pulsatility could be imaged in both cases, as can be seen, e.g., in Figure 6A,B,F,G. The PAH patient displayed a low but noticeable signal increase, homogeneously spread in the left and right lung parenchyma with NUFD that could not be noticed with FD: the CTEPH patient showed stronger signal intensities in areas of the lower and upper right lung.

Increased SNR becomes also apparent when comparing the perfusion signal delay maps from FD and NUFD. For the PAH patient (Figure 6D,E), the NUFD delay map shows a smoother signal delay than the FD map, whose phase estimate is strongly distorted by noise.

5 | DISCUSSION

In this work, a new method for pulmonary Fourier-decomposition MRI based on the nonuniform Fourier transform was presented and applied for visualizing signal amplitudes and quantifying the signal delay in the lungs. It was demonstrated that, by adding a frequency-tracking step to the original FD method and switching perspective from variable signal frequency to variable sampling frequency, spectrally spread-out

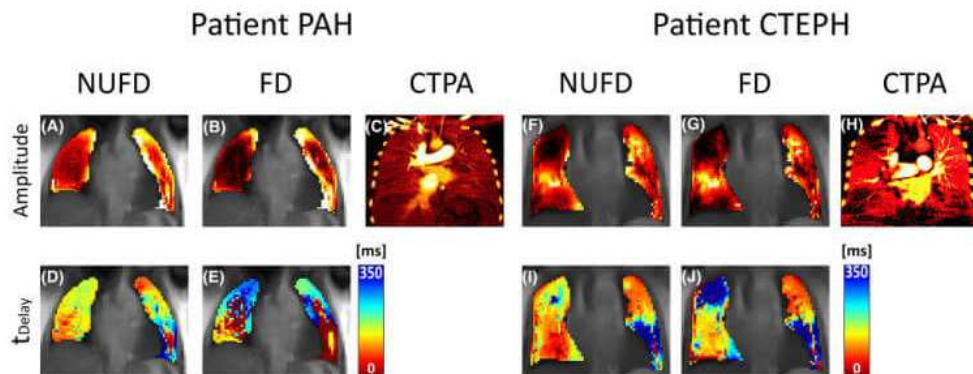


FIGURE 6 Perfusion-weighted NUFD and FD maps of patients with suspected PAH and CTEPH. A,B,F,G, FD and NUFD perfusion-weighted amplitude maps. D,E,I,J, Perfusion time delay maps. C,H, These 2 patients also had iodine-enhanced dual-energy CT pulmonary angiogram (CTPA) measurements (100/140Sn kV, 165/140 mAs, pitch = 1.2 for PAH patient and 90/150Sn kV, 60/46 mAs, pitch = 1.2 for CTEPH patient) performed as part of clinical routine within 3 months of their MR scans. The comparison shows that perfusion signal improvements from NUFD coincides better with displayed iodine concentration in both CTPA images. For the CTEPH patient, the CTPA image displays the decreasing, yet still existing signal intensity in the upper and lower part of the right lung where the lower part is stronger than the upper. This coincides better with the NUFD perfusion amplitude map than the one generated with FD

signal contribution could be collected onto a single frequency bin. This led to lessened bin spread caused by frequency variability as well as significant increase of SNR in both healthy test subjects and patient measurements, which can be expected to translate into more reliable quantitative results and less noisy parameter maps.

The patient measurements shown in Figure 6 clearly exemplify the difference NUFD can make for the evaluation of functional maps compared to FD. The effects are especially illustrated in the time delay maps comparing NUFD and FD, in which the PAH patient (Figure 6D,E) showed smoother progression and the CTEPH patient displayed further subtleties with better detectable signal progression (Figure 6L,J) in the upper right lung. In both cases, SNR was significantly improved. In the amplitude maps of the PAH patient (Figure 6A,B), the signal was substantially raised in voxels that had signal close to or lower than the noise floor (i.e., the local noise level of these voxels) with the FD method.

A key step of our new approach is frequency tracking of either the respiratory or the cardiac frequency during the 1 to 2 min of measurement. Current signal processing studies still discuss how best to describe signals with varying frequencies as amalgamation of multiple components and have specifically highlighted the influence of variable signal amplitudes.²² Variable amplitudes are expected in biological signal variations (especially for ventilation-associated signals) and must be dealt with to avoid misleading added low frequency components. With this in mind, the SWT method was selected due to its implementation where a variable amplitude factor is added to the regular wavelet transform definition. In addition, SWT has also been shown to offer improved frequency localization in time compared with regular continuous wavelet transform.²³ The resulting time-frequency representation of the SWT approach also helps to spread out potential artifacts and noise over the 2D frequency-time spectrum resulting in more stable estimates than those performed only in the (1D) time domain.

Because the NUFD method requires no changes in image acquisition parameters, it can easily be implemented as a complement to ongoing and future studies. The tracking of the (free-breathing) respiratory frequency offers fewer limitations for patient selection compared to regular FD MRI, as even patients strongly suffering from their conditions, which have troubles to breathe regularly, can be examined.

Due to the possibility of determining the signal delay with high temporal resolution from phase estimates, time delay maps can be calculated to estimate how the perfusion or respiratory signal propagates through microstructures in the lungs. However, further studies are required to validate the resulting delay maps quantitatively. The measured range of ventilation delays throughout the lungs of healthy subjects was between approximately 180 and 370 ms. This agrees well with results

from a dynamic spiral MRI study,²⁴ in which similar values were shown for the gas delay during inhalation.

Similar to PREFUL¹⁰ and SENCEFUL,⁹ the proposed NUFD method generates functional maps where all of the signal contribution collected during the measurement can be used. Because the same amount of signal is used for the evaluation, one would expect similar SNR increases with the NUFD approach as with the 2 other methods compared to FD. NUFD MRI, however, distinguishes itself in that it does not require exact phase estimates for performing image or k-space line resorting, thus simplifying the final implementation.

There are some limitations of this study. First, the proposed NUFD approach requires an additional (in comparison to FD MRI) frequency-tracking step. There exist several approaches for frequency tracking and here we used the SWT in combination with ridge detection. Further studies should compare this technique with other approaches (such as, e.g., frequency tracking by simple peak finding) to determine the most robust and reliable technique. Second, even without frequency variability, NUFD MRI can suffer from the same amplitude stability issues as was described for FD MRI,²⁵ for which solutions such as windowing²¹ or matrix pencil decomposition,²⁵ are readily available. Thus, NUFD estimates of both amplitude and phase can be expected to be further improved upon with an optimal choice of a filtering window function. However, because the focus of this study was to compare the results between NUFD and FD MRI (where windowing is not an efficient option due to the predominant influence of frequency variability in vivo), this was left out for future investigations. Furthermore, this is a proof of principle study and future studies with larger sample size are required to establish clinical relevance of the found SNR improvements. Finally, it should be noted that because imaging is performed in 2D, artifacts can occur as with the regular FD method due to movement of structures in an out of the slice which would likely occur at ventilation rate.

6 | CONCLUSIONS

This study presents a modification of functional Fourier-decomposition lung imaging with frequency-adapted Fourier transform to compensate for variability in perfusion and ventilation frequency. We demonstrated that using nonuniform Fourier transform in combination with frequency tracking can significantly increase SNR and reduce frequency overlaps by collecting the signal intensity onto single frequency bins.

ACKNOWLEDGMENT

We thank Dr. Oliver Bieri (Universitätsspital Basel, Switzerland) for his work on optimizing the uf-bSSFP sequence.

CONFLICT OF INTEREST

Thomas Gaass is currently employed by Siemens Healthcare Pty Ltd, Bowen Hills, Australia. Bernd Kühn is currently employed by Siemens Healthcare GmbH, Erlangen, Germany.

ENDNOTES

^a Generally, 3 types of NUFFT algorithms are differentiated: (1) Type-1 NUFFTs perform a spectral analysis of data sampled at nonequidistant time points resulting in an equidistantly defined frequency spectrum; (2) type-2 NUFFTs perform a spectral analysis of equidistantly sampled data resulting in a nonequidistantly defined frequency spectrum; (3) type-3 NUFFTs combine type-1 and type-2 NUFFT, namely transforming a nonequidistantly sampled signal to a nonequidistantly defined frequency spectrum.

^b Code initially written by M. Ferrara at AFRL Sensors Directorate Innovative Algorithms Branch.

REFERENCES

- Bauman G, Puderbach M, Deimling M, et al. Non-contrast-enhanced perfusion and ventilation assessment of the human lung by means of Fourier decomposition in proton MRI. *Magn Reson Med*. 2009;62:656–664.
- Kjørstad Å, Corteville DMR, Fischer A, et al. Quantitative lung perfusion evaluation using Fourier decomposition perfusion MRI. *Magn Reson Med*. 2014;72:558–562.
- Zapke M, Topf H-G, Zenker M, et al. Magnetic resonance lung function—a breakthrough for lung imaging and functional assessment? A phantom study and clinical trial. *Respir Res*. 2006;7:106.
- Martirosian P, Boss A, Fenchel M, et al. Quantitative lung perfusion mapping at 0.2 T using FAIR True-FISP MRI. *Magn Reson Med*. 2006;55:1065–1074.
- Bauman G, Scholz A, Rivoire J, et al. Lung ventilation- and perfusion-weighted Fourier decomposition magnetic resonance imaging: in vivo validation with hyperpolarized ³He and dynamic contrast-enhanced MRI. *Magn Reson Med*. 2013;69:229–237.
- Bauman G, Lützen U, Ullrich M, et al. Pulmonary functional imaging: qualitative comparison of Fourier decomposition MR imaging with SPECT/CT in porcine lung. *Radiology*. 2011;260:551–559.
- Bauman G, Eichinger M, Uecker M. High temporal resolution radial bSSFP sequence with nonlinear inverse reconstruction for the measurement of the pulmonary blood inflow time using Fourier decomposition MRI. In: Proceedings of the 20th Annual Meeting of ISMRM, Melbourne, Australia, 2012. Abstract 1340.
- Veldhoen S, Weng AM, Wirth C, et al. Pulmonary phase imaging using self-gated Fourier decomposition MRI in patients with cystic fibrosis. In: Proceedings of the 24th Annual Meeting of ISMRM, Singapore, 2016. Abstract 114.
- Fischer A, Weick S, Ritter CO, et al. Self-gated Non-Contrast-Enhanced Functional Lung imaging (SENCEFUL) using a quasi-random fast low-angle shot (FLASH) sequence and proton MRI. *NMR Biomed*. 2014;27:907–917.
- Voskrebenezv A, Gutberlet M, Klimeš F, et al. Feasibility of quantitative regional ventilation and perfusion mapping with phase-resolved functional lung (PREFUL) MRI in healthy volunteers and COPD, CTEPH, and CF patients. *Magn Reson Med*. 2018;79:2306–2314.
- Bieri O. Ultra-fast steady state free precession and its application to in vivo (1)H morphological and functional lung imaging at 1.5 tesla. *Magn Reson Med*. 2013;70:657–663.
- Hirsch JA, Bishop B. Respiratory sinus arrhythmia in humans: how breathing pattern modulates heart rate. *Am J Physiol*. 1981;241:H620–H629.
- Chefd'hotel C, Hermsillo G, Faugeras O. Flows of diffeomorphisms for multimodal image registration. In: Proceedings IEEE International Symposium on Biomedical Imaging, Washington, DC, 2002:753–756.
- Chefd'Hotel C, Hermsillo G, Faugeras O. A variational approach to multi-modal image matching. In: Proceedings IEEE Workshop on Variational and Level Set Methods in Computer Vision, Vancouver, BC, Canada, 2001:21–28.
- Daubechies I, Lu J, Wu H-T. Synchrosqueezed wavelet transforms: an empirical mode decomposition-like tool. *Appl Comput Harmon Anal*. 2011;30:243–261.
- Carmona RA, Hwang WL, Torresani B. Characterization of signals by the ridges of their wavelet transforms. *IEEE Trans Signal Process*. 1997;45:2586–2590.
- Greengard L, Lee J. Accelerating the nonuniform fast Fourier transform. *SIAM Rev*. 2004;46:443–454.
- Liu QH, Nguyen N. An accurate algorithm for nonuniform fast Fourier transforms (NUFFT's). *IEEE Microw Guid Wave Lett*. 1998;8:18–20.
- Zhang K, Kang JU. Graphics processing unit accelerated non-uniform fast Fourier transform for ultrahigh-speed, real-time Fourier-domain OCT. *Opt Express*. 2010;18:23472.
- Goldstein RM, Zebker HA, Werner CL. Satellite radar interferometry: two-dimensional phase unwrapping. *Radio Sci*. 1988;23:713–720.
- Harris FJ. On the use of windows for harmonic analysis with the discrete Fourier transform. *Proc IEEE*. 1978;66:51–83.
- Huang NE, Shen Z, Long SR, et al. The empirical mode decomposition and the Hilbert spectrum for nonlinear and non-stationary time series analysis. *Proc R Soc Lond Math Phys Eng Sci*. 1998;454:903–995.
- Thakur G, Brevdo E, Fučkar NS, Wu H-T. The Synchrosqueezing algorithm for time-varying spectral analysis: robustness properties and new paleoclimate applications. *Signal Process*. 2013;93:1079–1094.
- Salerno M, Altes TA, Brookeman JR, de Lange EE, Mugler JP. Dynamic spiral MRI of pulmonary gas flow using hyperpolarized (³He): preliminary studies in healthy and diseased lungs. *Magn Reson Med*. 2001;46:667–677.
- Bauman G, Bieri O. Matrix pencil decomposition of time-resolved proton MRI for robust and improved assessment of pulmonary ventilation and perfusion. *Magn Reson Med*. 2017;77:336–342.

How to cite this article: Bondesson D, Schneider MJ, Gaass T, et al. Nonuniform Fourier-decomposition MRI for ventilation- and perfusion-weighted imaging of the lung. *Magn Reson Med*. 2019;82:1312–1321. <https://doi.org/10.1002/mrm.27803>

4. Additional Contributions

4.1 Silbernagel E, Bondesson D, Behr J, Dinkel J, Reichenberger F. Taking another view on lung fibrosis. *Am J Respir Crit Care Med* 2018;197:947–948. <https://www.atsjournals.org/doi/10.1164/rccm.201708-1683IM>

IMAGES IN PULMONARY, CRITICAL CARE, SLEEP MEDICINE AND THE SCIENCES

Taking Another View on Lung Fibrosis

Edith Silbernagel^{1*}, David Bondesson^{2*}, Juergen Behr^{1,3}, Julien Dinkel^{1,2}, and Frank Reichenberger¹

¹Asklepios Lung-Center Munich-Gauting, ²Department of Radiology, and ³Department of Internal Medicine V, Ludwig Maximilians University LMU Hospital Munich, Comprehensive Pneumology Center, Munich, Germany

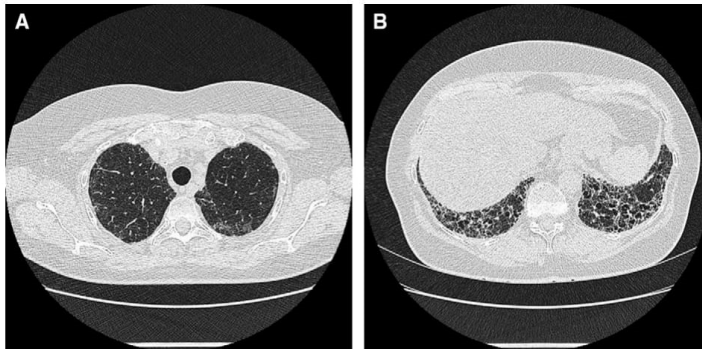


Figure 1. (A) High-resolution computed tomography imaging of the upper lobe, normal lung tissue (1-mm slice). (B) High-resolution computed tomography of the lower lobe, fibrotic lung tissue (1-mm slice).

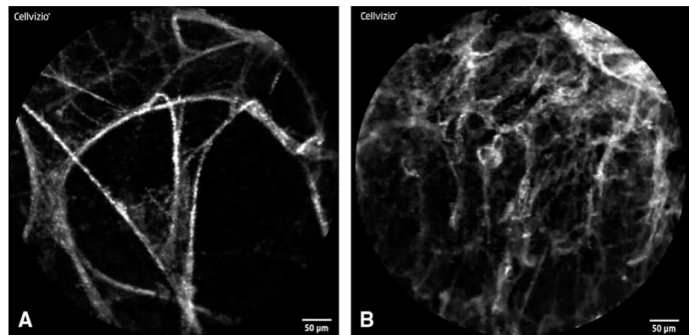


Figure 2. (A) Probe-based confocal laser endomicroscopy imaging of the upper lobe, normal lung tissue. (B) Probe-based confocal laser endomicroscopy imaging of the lower lobe, fibrotic lung tissue.

extract a topological skeleton of the fiber structures. The topological connectivity was calculated using the Euler characteristics (4) (Figures 4A and 4B). Although fiber thickness enables assessment of an average density of alveolar structures by color transformation, topological connectivity is a measure of networking of elastic fibers within the alveolar compartment.

A 61-year-old woman was admitted to the hospital for an assessment of interstitial lung disease. She presented with bilateral basal crackles but had an otherwise uneventful medical history, especially with regard to environmental exposure, medication, or rheumatic disorders.

High-resolution thoracic computed tomography showed reticular changes and honeycombing in the basal segments of the lower lung fields (Figure 1B), but normal lung tissue in the upper lobes (Figure 1A), consistent with usual interstitial pneumonia pattern.

The patient underwent bronchoscopy with probe-based confocal laser endomicroscopy (Cellvizio; Mauna Kea Technologies) for *in vivo* imaging of the alveolar compartment. This technique is based on laser-induced autofluorescence of elastic fibers using a miniature probe that enables tissue visualization at the microscopic level (1).

In the upper lobe (segment 3), normal alveolar architecture was observed (Figure 2A); however, in the lower lobe (segment 9), there was severe destruction and distortion of the alveolar compartment (Figure 2B).

To generate qualitative images, image stack data were initially binarized using a manually selected threshold; this was then followed by the segmentation of connecting structures using ImageJ/BoneJ (www.bonej.org) (2). Average fiber thickness was calculated within localized maps, using a cylinder fitting algorithm (3) (Figures 3A and 3B). A medial surface/axis thinning algorithm was used to

*These authors contributed equally to the manuscript.

Author Contributions: Design, concept, and performing analysis: E.S. and F.R.; post-processing and analysis: D.B. and J.D.; and analysis and interpretation: E.S., J.B., J.D., and F.R.

Am J Respir Crit Care Med Vol 197, Iss 7, pp 947–948, Apr 1, 2018
Copyright © 2018 by the American Thoracic Society
Originally Published in Press as DOI: 10.1164/rccm.201708-1683IM on February 2, 2018
Internet address: www.atsjournals.org

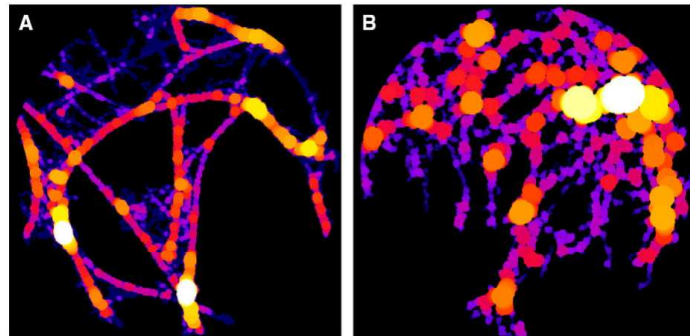


Figure 3. (A) Thickness imaging of the upper lobe, normal lung tissue. Fiber thickness = 13.8. (B) Thickness imaging of the lower lobe, fibrotic lung tissue. Fiber thickness = 31.1.

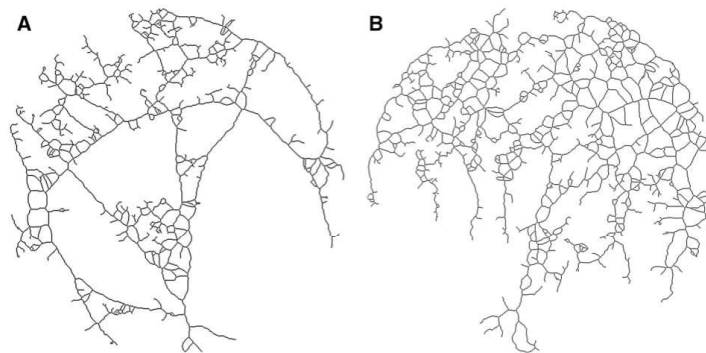


Figure 4. (A) Topologically conserved skeleton imaging of the upper lobe, normal lung tissue, topological connectivity = 91.3. (B) Topologically conserved skeleton imaging of the lower lobe, fibrotic lung tissue, topological connectivity = 13.5.

At this time, imaging in lung fibrosis is mainly restricted to high-resolution thoracic computed tomography scan. Probe-based confocal laser endomicroscopy and image postprocessing enables *in vivo* visualization of alveolar structures with description and quantification of changes in lung parenchyma that have the potential to influence the differential diagnosis in interstitial lung disease.

This work was presented as a poster at the American Thoracic Society 2016 International Conference (5). ■

Author disclosures are available with the text of this article at www.atsjournals.org.

References

1. Thiberville L, Salaün M, Bourg-Heckly G. In vivo confocal microendoscopy: from the proximal bronchus down to the pulmonary acinus. *Eur Respir Monogr* 2010;48:73–89.
2. Doube M, Klosowski MM, Arganda-Carreras I, Cordelières FP, Dougherty RP, Jackson JS, et al. BoneJ: Free and extensible bone image analysis in ImageJ. *Bone* 2010;47:1076–1079.
3. Dougherty R, Kunzelmann K. Computing local thickness of 3D structures with ImageJ. *Microsc Microanal* 2007;13:1678–1679.
4. Lee TC, Kashyap RL, Chu CN. Building skeleton models via 3-D medial surface axis thinning algorithms. *CVGIP Graph Models Image Process* 1994;56:462–478.
5. Bondesson D, Gaass T, Behr J, Reichenberger F, Dinkel J, Silbernager E. Automated quantitative evaluation of alveolar structure on confocal laser endomicroscopy [abstract]. *Am J Respir Crit Care Med* 2016; 193:A7527.

Reprinted with permission of the American Thoracic Society.

Copyright © 2020 American Thoracic Society. All rights reserved.

Cite: Silbernagel E, Bondesson D, Behr J, Dinkel J, Reichenberger F. Taking another view on lung fibrosis. *Am J Respir Crit Care Med* 2018;197:947–948.

The American Journal of Respiratory and Critical Care Medicine is an official journal of the American Thoracic Society.

5. List of abbreviations

B	Magnetic field
bSSFP	Balanced steady state free precession (sequence)
COP	Cryptogenic organizing pneumonia
CT	Computer tomography
CTEPH	Chronic thromboembolic disease
CTPA	CT pulmonary angiography
CWT	Continuous wavelet transform
DPLD	Diffuse parenchymal lung disease
E	Energy difference between two populations of spins
FFT	Fast Fourier transform
FOV	Field of view
FD	Fourier decomposition
G	Magnetic gradient field
HP	Hypersensitive pneumonitis
HRCT	High resolution CT
I	Quantum magnetic spin property
ILD	Interstitial lung disease
IPF	Idiopathic pulmonary fibrosis
M	Macro-net magnetization
MRI	Magnetic resonance imaging
MRMR	Minimal redundancy and maximum relevancy
NMR	Nuclear magnetic resonance
NSIP	Non-specific interstitial pneumonia
NUFD	Non-uniform Fourier decomposition
PAH	Pulmonary arterial hypertension

PCLE	Probe-based confocal laser endomicroscopy
PH	Pulmonary hypertension
RF	radiofrequency (pulse)
S	Recorded signal
SNR	Signal-to-noise ratio
SOI	Structure of interest
T	Temperature/time
TE	Echo time
TR	Repetition time
V/Q	Ventilation/perfusion (scan)
X-ray	Chest radiography
Z	Atomic number
α	The total flip angle of the net magnetization
μ	Magnetic moment of the nucleus
φ	Phase of the transverse magnetization
ω_0	Larmor frequency
ρ	Spin density
γ	Particle-specific gyromagnetic ratio

6. References

1. Bates DV, Hansen-Flaschen J. Respiratory disease. *Encycl Br at* <<https://www.britannica.com/science/respiratory-disease>>.
2. Ferkol T, Schraufnagel D. The Global Burden of Respiratory Disease. *Ann Am Thorac Soc* 2014;11:404–406.
3. Welte T. Imaging in the Diagnosis of Lung Disease. *Dtsch Ärztebl Int* 2014;111:179–180.
4. Wielpütz MO, Heußel CP, Herth FJF, Kauczor H-U. Radiological Diagnosis in Lung Disease. *Dtsch Ärztebl Int* 2014;111:181–187.
5. van Beek EJ, Hoffman EA. Functional Imaging: CT and MRI. *Clin Chest Med* 2008;29:195–vii.
6. Biederer J, Beer M, Hirsch W, Wild J, Fabel M, Puderbach M, Van Beek EJR. MRI of the lung (2/3). Why ... when ... how? *Insights Imaging* 2012;3:355–371.
7. Zapke M, Topf H-G, Zenker M, Kuth R, Deimling M, Kreisler P, Rauh M, Chefd'hotel C, Geiger B, Rupprecht T. Magnetic resonance lung function--a breakthrough for lung imaging and functional assessment? A phantom study and clinical trial. *Respir Res* 2006;7:106.
8. Bauman G, Puderbach M, Heimann T, Kopp-Schneider A, Fritzsching E, Mall MA, Eichinger M. Validation of Fourier decomposition MRI with dynamic contrast-enhanced MRI using visual and automated scoring of pulmonary perfusion in young cystic fibrosis patients. *Eur J Radiol* 2013;82:2371–2377.
9. Bauman G, Scholz A, Rivoire J, Terekhov M, Friedrich J, de Oliveira A, Semmler W, Schreiber LM, Puderbach M. Lung ventilation- and perfusion-weighted Fourier decomposition magnetic resonance imaging: in vivo validation with hyperpolarized ^3He and dynamic contrast-enhanced MRI. *Magn Reson Med* 2013;69:229–237.
10. Schönfeld C, Cebotari S, Voskrebenezv A, Gutberlet M, Hinrichs J, Renne J, Hoepfer MM, Olsson KM, Welte T, Wacker F, Vogel-Claussen J. Performance of perfusion-weighted Fourier decomposition MRI for detection of chronic pulmonary emboli. *J Magn Reson Imaging* 2015;42:72–79.

11. Colella S, Haentschel M, Shah P, Poletti V, Hetzel J. Transbronchial Lung Cryobiopsy in Interstitial Lung Diseases: Best Practice. *Respir Int Rev Thorac Dis* 2018;95:383–391.
12. Panchabhai TS, Mehta AC. Historical Perspectives of Bronchoscopy. Connecting the Dots. *Ann Am Thorac Soc* 2015;12:631–641.
13. Qureshi RA, Ahmed TA, Grayson AD, Soorae AS, Drakeley MJ, Page RD. Does lung biopsy help patients with interstitial lung disease? *Eur J Cardiothorac Surg* 2002;21:621–626.
14. Jeffery P, Holgate S, Wenzel S, Endobronchial Biopsy Workshop. Methods for the assessment of endobronchial biopsies in clinical research: application to studies of pathogenesis and the effects of treatment. *Am J Respir Crit Care Med* 2003;168:S1-17.
15. Thiberville L, Moreno-Swirc S, Vercauteren T, Peltier E, Cavé C, Bourg Heckly G. In Vivo Imaging of the Bronchial Wall Microstructure Using Fibered Confocal Fluorescence Microscopy. *Am J Respir Crit Care Med* 2007;175:22–31.
16. A Patient's Guide to Respiratory Disease. *US News World Rep* at <<https://health.usnews.com/conditions/respiratory-disease>>.
17. Shlobin OA, Brown AW, Nathan SD. Pulmonary Hypertension in Diffuse Parenchymal Lung Diseases. *CHEST* 2017;151:204–214.
18. Walters EH, Du Bois RM. *Immunology and management of interstitial lung diseases: a clinician's guide*. London; New York: Chapman & Hall Medical; 1995.
19. Coultas DB, Zumwalt RE, Black WC, Sobonya RE. The epidemiology of interstitial lung diseases. *Am J Respir Crit Care Med* 1994;150:967–972.
20. Huapaya JA, Wilfong EM, Harden CT, Brower RG, Danoff SK. Risk factors for mortality and mortality rates in interstitial lung disease patients in the intensive care unit. *Eur Respir Rev* 2018;27:.
21. Travis WD, Costabel U, Hansell DM, King TE, Lynch DA, Nicholson AG, Ryerson CJ, Ryu JH, Selman M, Wells AU, Behr J, Bouros D, Brown KK, Colby TV, Collard HR, Cordeiro CR, Cottin V, Crestani B, Drent M, Dudden RF, Egan J, Flaherty K, Hogaboam C, Inoue Y, Johkoh T,

- Kim DS, Kitaichi M, Loyd J, Martinez FJ, *et al.* An Official American Thoracic Society/European Respiratory Society Statement: Update of the International Multidisciplinary Classification of the Idiopathic Interstitial Pneumonias. *Am J Respir Crit Care Med* 2013;188:733–748.
22. Wells AU. High-Resolution Computed Tomography in the Diagnosis of Diffuse Lung Disease: A Clinical Perspective. *Semin Respir Crit Care Med* 2003;24:347–356.
23. Padley SP, Hansell DM, Flower CD, Jennings P. Comparative accuracy of high resolution computed tomography and chest radiography in the diagnosis of chronic diffuse infiltrative lung disease. *Clin Radiol* 1991;44:222–226.
24. Mathieson JR, Mayo JR, Staples CA, Müller NL. Chronic diffuse infiltrative lung disease: comparison of diagnostic accuracy of CT and chest radiography. *Radiology* 1989;171:111–116.
25. Demedts M, Behr J, Buhl R, Costabel U, Dekhuijzen R, Jansen HM, MacNee W, Thomeer M, Wallaert B, Laurent F, Nicholson AG, Verbeken EK, Verschakelen J, Flower CDR, Capron F, Petruzzelli S, De Vuyst P, van den Bosch JMM, Rodriguez-Becerra E, Corvasce G, Lankhorst I, Sardina M, Montanari M. High-Dose Acetylcysteine in Idiopathic Pulmonary Fibrosis. *N Engl J Med* 2005;353:2229–2242.
26. Elicker BM, Kallianos KG, Henry TS. The role of high-resolution computed tomography in the follow-up of diffuse lung disease: Number 2 in the Series “Radiology” Edited by Nicola Sverzellati and Sujal Desai. *Eur Respir Rev* 2017;26:.
27. Iwasawa T, Ogura T, Sakai F, Kanauchi T, Komagata T, Baba T, Gotoh T, Morita S, Yazawa T, Inoue T. CT analysis of the effect of pirfenidone in patients with idiopathic pulmonary fibrosis. *Eur J Radiol* 2014;83:32–38.
28. American Thoracic Society/European Respiratory Society International Multidisciplinary Consensus Classification of the Idiopathic Interstitial Pneumonias. *Am J Respir Crit Care Med* 2002;165:277–304.
29. Bradley B, Branley HM, Egan JJ, Greaves MS, Hansell DM, Harrison NK, Hirani N, Hubbard R, Lake F, Millar AB, Wallace W a. H, Wells AU, Whyte MK, Wilsher ML, British Thoracic

Society Interstitial Lung Disease Guideline Group, British Thoracic Society Standards of Care Committee, Thoracic Society of Australia, New Zealand Thoracic Society, Irish Thoracic Society. Interstitial lung disease guideline: the British Thoracic Society in collaboration with the Thoracic Society of Australia and New Zealand and the Irish Thoracic Society. *Thorax* 2008;63 Suppl 5:v1-58.

30. Raghu G, Collard HR, Egan JJ, Martinez FJ, Behr J, Brown KK, Colby TV, Cordier J-F, Flaherty KR, Lasky JA, Lynch DA, Ryu JH, Swigris JJ, Wells AU, Ancochea J, Bouros D, Carvalho C, Costabel U, Ebina M, Hansell DM, Johkoh T, Kim DS, King TE, Kondoh Y, Myers J, Müller NL, Nicholson AG, Richeldi L, Selman M, *et al.* An Official ATS/ERS/JRS/ALAT Statement: Idiopathic Pulmonary Fibrosis: Evidence-based Guidelines for Diagnosis and Management. *Am J Respir Crit Care Med* 2011;183:788–824.
31. Strange G, Playford D, Stewart S, Deague JA, Nelson H, Kent A, Gabbay E. Pulmonary hypertension: prevalence and mortality in the Armadale echocardiography cohort. *Heart Br Card Soc* 2012;98:1805–1811.
32. Peacock AJ, Murphy NF, McMurray JJV, Caballero L, Stewart S. An epidemiological study of pulmonary arterial hypertension. *Eur Respir J* 2007;30:104–109.
33. Ling Y, Johnson MK, Kiely DG, Condliffe R, Elliot CA, Gibbs JSR, Howard LS, Pepke-Zaba J, Sheares KKK, Corris PA, Fisher AJ, Lordan JL, Gaine S, Coghlan JG, Wort SJ, Gatzoulis MA, Peacock AJ. Changing demographics, epidemiology, and survival of incident pulmonary arterial hypertension: results from the pulmonary hypertension registry of the United Kingdom and Ireland. *Am J Respir Crit Care Med* 2012;186:790–796.
34. Humbert M, Sitbon O, Chaouat A, Bertocchi M, Habib G, Gressin V, Yaici A, Weitzenblum E, Cordier J-F, Chabot F, Dromer C, Pison C, Reynaud-Gaubert M, Haloun A, Laurent M, Hachulla E, Simonneau G. Pulmonary arterial hypertension in France: results from a national registry. *Am J Respir Crit Care Med* 2006;173:1023–1030.

35. Gall H, Hoeper MM, Richter MJ, Cacheris W, Hinzmann B, Mayer E. An epidemiological analysis of the burden of chronic thromboembolic pulmonary hypertension in the USA, Europe and Japan. *Eur Respir Rev* 2017;26:.
36. Badesch DB, Raskob GE, Elliott CG, Krichman AM, Farber HW, Frost AE, Barst RJ, Benza RL, Liou TG, Turner M, Giles S, Feldkircher K, Miller DP, McGoon MD. Pulmonary arterial hypertension: baseline characteristics from the REVEAL Registry. *Chest* 2010;137:376–387.
37. Simonneau G, Galiè N, Rubin LJ, Langleben D, Seeger W, Domenighetti G, Gibbs S, Lebrech D, Speich R, Beghetti M, Rich S, Fishman A. Clinical classification of pulmonary hypertension. *J Am Coll Cardiol* 2004;43:S5–S12.
38. Tudor RM, Marecki JC, Richter A, Fijalkowska I, Flores S. Pathology of pulmonary hypertension. *Clin Chest Med* 2007;28:23–42, vii.
39. D’Alonzo GE, Barst RJ, Ayres SM, Bergofsky EH, Brundage BH, Detre KM, Fishman AP, Goldring RM, Groves BM, Kernis JT. Survival in patients with primary pulmonary hypertension. Results from a national prospective registry. *Ann Intern Med* 1991;115:343–349.
40. Galiè N, Humbert M, Vachiery J-L, Gibbs S, Lang I, Torbicki A, Simonneau G, Peacock A, Noordegraaf AV, Beghetti M, Ghofrani A, Sanchez MAG, Hansmann G, Klepetko W, Lancellotti P, Matucci M, McDonagh T, Pierard LA, Trindade PT, Zompatori M, Hoeper M. 2015 ESC/ERS Guidelines for the diagnosis and treatment of pulmonary hypertension: The Joint Task Force for the Diagnosis and Treatment of Pulmonary Hypertension of the European Society of Cardiology (ESC) and the European Respiratory Society (ERS) Endorsed by: Association for European Paediatric and Congenital Cardiology (AEPC), International Society for Heart and Lung Transplantation (ISHLT). *Eur Respir J* 2015;46:903–975.
41. Rengier F, Melzig C, Derlin T, Marra AM, Vogel-Claussen J. Advanced imaging in pulmonary hypertension: emerging techniques and applications. *Int J Cardiovasc Imaging* 2019;35:1407–1420.

42. He J, Fang W, Lv B, He J-G, Xiong C-M, Liu Z-H, He Z-X. Diagnosis of chronic thromboembolic pulmonary hypertension: comparison of ventilation/perfusion scanning and multidetector computed tomography pulmonary angiography with pulmonary angiography. *Nucl Med Commun* 2012;33:459–463.
43. Johns CS, Swift AJ, Rajaram S, Hughes PJC, Capener DJ, Kiely DG, Wild JM. Lung perfusion: MRI vs. SPECT for screening in suspected chronic thromboembolic pulmonary hypertension. *J Magn Reson Imaging JMRI* 2017;46:1693–1697.
44. Rajaram S, Swift AJ, Telfer A, Hurdman J, Marshall H, Lorenz E, Capener D, Davies C, Hill C, Elliot C, Condliffe R, Wild JM, Kiely DG. 3D contrast-enhanced lung perfusion MRI is an effective screening tool for chronic thromboembolic pulmonary hypertension: results from the ASPIRE Registry. *Thorax* 2013;68:677–678.
45. Bauman G, Lützen U, Ullrich M, Gaass T, Dinkel J, Elke G, Meybohm P, Frerichs I, Hoffmann B, Borggreffe J, Knuth H-C, Schupp J, Prüm H, Eichinger M, Puderbach M, Biederer J, Hintze C. Pulmonary functional imaging: qualitative comparison of Fourier decomposition MR imaging with SPECT/CT in porcine lung. *Radiology* 2011;260:551–559.
46. Voskrebenezv A, Gutberlet M, Klimeš F, Kaireit TF, Schönfeld C, Rotärmel A, Wacker F, Vogel-Claussen J. Feasibility of quantitative regional ventilation and perfusion mapping with phase-resolved functional lung (PREFUL) MRI in healthy volunteers and COPD, CTEPH, and CF patients. *Magn Reson Med* 2017;doi:10.1002/mrm.26893.
47. Schoenfeld C, Cebotari S, Hinrichs J, Renne J, Kaireit T, Olsson KM, Voskrebenezv A, Gutberlet M, Hoepfer MM, Welte T, Haverich A, Wacker F, Vogel-Claussen J. MR Imaging–derived Regional Pulmonary Parenchymal Perfusion and Cardiac Function for Monitoring Patients with Chronic Thromboembolic Pulmonary Hypertension before and after Pulmonary Endarterectomy. *Radiology* 2015;279:925–934.
48. Schoenfeld C, Hinrichs JB, Olsson KM, Kuettner M-A, Renne J, Kaireit T, Czerner C, Wacker F, Hoepfer MM, Meyer BC, Vogel-Claussen J. Cardio-pulmonary MRI for detection of

- treatment response after a single BPA treatment session in CTEPH patients. *Eur Radiol* 2019;29:1693–1702.
49. Prybylski JP, Semelka RC, Jay M. The stability of gadolinium-based contrast agents in human serum: A reanalysis of literature data and association with clinical outcomes. *Magn Reson Imaging* 2017;38:145–151.
 50. Huckle JE, Altun E, Jay M, Semelka RC. Gadolinium Deposition in Humans: When Did We Learn That Gadolinium Was Deposited In Vivo? *Invest Radiol* 2016;51:236–240.
 51. Goualher GL, Perchant A, Genet M, Cavé C, Viellerobe B, Berier F, Abrat B, Ayache N. Towards Optical Biopsies with an Integrated Fibered Confocal Fluorescence Microscope. *Med Image Comput Comput-Assist Interv – MICCAI 2004* Springer, Berlin, Heidelberg; 2004. p. 761–768. doi:10.1007/978-3-540-30136-3_93.
 52. Lee P, Brokx HAP, Postmus PE, Sutedia TG. Dual digital video-autofluorescence imaging for detection of pre-neoplastic lesions. *Lung Cancer Amst Neth* 2007;58:44–49.
 53. Ikeda N, Hayashi A, Iwasaki K, Honda H, Tsuboi M, Usuda J, Kato H. Comprehensive diagnostic bronchoscopy of central type early stage lung cancer. *Lung Cancer* 2007;56:295–302.
 54. Thiberville L, Salaün M. Bronchoscopic Advances: On the Way to the Cells. *Respiration* 2010;79:441–449.
 55. Newton RC, Kemp SV, Yang G-Z, Elson DS, Darzi A, Shah PL. Imaging parenchymal lung diseases with confocal endomicroscopy. *Respir Med* 2012;106:127–137.
 56. Wellikoff AS, Holladay RC, Downie GH, Chaudoir CS, Brandi L, Turbat-Herrera EA. Comparison of in vivo probe-based confocal laser endomicroscopy with histopathology in lung cancer: A move toward optical biopsy. *Respirology* 2015;20:967–974.
 57. Filner JJ, Bonura EJ, Lau ST, Abounasr KK, Naidich D, Morice RC, Eapen GA, Jimenez CA, Casal RF, Ost D. Bronchoscopic Fibered Confocal Fluorescence Microscopy Image Characteristics and Pathologic Correlations. *J Bronchol Interv Pulmonol* 2011;18:23.

58. Yick CY, von der Thüsen JH, Bel EH, Sterk PJ, Kunst PW. In vivo imaging of the airway wall in asthma: fibered confocal fluorescence microscopy in relation to histology and lung function. *Respir Res* 2011;12:85.
59. Yserbyt J, Doods C, Decramer M, Verleden GM. Probe-based confocal laser endomicroscopy of the respiratory tract: A data consistency analysis. *Respir Med* 2013;107:1234–1240.
60. Meng P, Tan GL, Low SY, Takan A, Ng YL, Anantham D. Fibred confocal fluorescence microscopy in the diagnosis of interstitial lung diseases. *J Thorac Dis* 2016;8:3505-3514–3514.
61. Salaün M, Guisier F, Dominique S, Genevois A, Jounieaux V, Bergot E, Thill C, Piton N, Thiberville L. In vivo probe-based confocal laser endomicroscopy in chronic interstitial lung diseases: Specific descriptors and correlation with chest CT. *Respirology* 2019;24:783–791.
62. Yserbyt J, Doods C, Decramer M, Verleden GM. Acute lung allograft rejection: Diagnostic role of probe-based confocal laser endomicroscopy of the respiratory tract. *J Heart Lung Transplant* 2014;33:492–498.
63. Thiberville L, Salaun M, Lachkar S, Dominique S, Moreno-Swirc S, Vever-Bizet C, Bourgeois Heckly G. Human in vivo fluorescence microimaging of the alveolar ducts and sacs during bronchoscopy. *Eur Respir J* 2009;33:974–985.
64. Hildebrand T, Rügsegger P. A new method for the model-independent assessment of thickness in three-dimensional images. *J Microsc* 1997;185:67–75.
65. Pratt WK. *Digital Image Processing : PIKS Scientific inside*, 4th Edition. New York: John Wiley & Sons, INC; 2007. at https://www.academia.edu/30586970/Digital_Image_Processing_4th_Edition_-_William_K_Pratt.
66. Silbernagel E, Bondesson D, Behr J, Dinkel J, Reichenberger F. Taking Another View on Lung Fibrosis. *Am J Respir Crit Care Med* 2018;197:947–948.

67. Arganda-Carreras I, Kaynig V, Rueden C, Eliceiri KW, Schindelin J, Cardona A, Sebastian Seung H. Trainable Weka Segmentation: a machine learning tool for microscopy pixel classification. *Bioinformatics* 2017;33:2424–2426.
68. Cawley GC, Talbot NLC. On Over-fitting in Model Selection and Subsequent Selection Bias in Performance Evaluation. *J Mach Learn Res* 2010;11:2079–2107.
69. Fawcett T. An introduction to ROC analysis. *Pattern Recognit Lett* 2006;27:861–874.
70. Shlien S. Multiple binary decision tree classifiers. *Pattern Recognit* 1990;23:757–763.
71. Breiman L. Random Forests. *Mach Learn* 2001;45:5–32.
72. Dietterich TG. An Experimental Comparison of Three Methods for Constructing Ensembles of Decision Trees: Bagging, Boosting, and Randomization. *Mach Learn* 2000;40:139–157.
73. Buda M, Maki A, Mazurowski MA. A systematic study of the class imbalance problem in convolutional neural networks. *Neural Netw* 2018;106:249–259.
74. Bruzzone L, Serpico SB. Classification of imbalanced remote-sensing data by neural networks. *Pattern Recognit Lett* 1997;18:1323–1328.
75. Sokolova M, Lapalme G. A systematic analysis of performance measures for classification tasks. *Inf Process Manag* 2009;45:427–437.
76. Chawla NV, Bowyer KW, Hall LO, Kegelmeyer WP. SMOTE: Synthetic Minority Over-sampling Technique. *J Artif Intell Res* 2002;16:321–357.
77. Japkowicz N. The Class Imbalance Problem: Significance and Strategies. *Proc 2000 Int Conf Artif Intell ICAI* 2000. p. 111–117.
78. Arganda-Carreras I. *Trainable Weka Segmentation: a machine learning tool for microscopy pixel classification*. Oxford Univ Press; 2017.
79. Blum AL, Langley P. Selection of relevant features and examples in machine learning. *Artif Intell* 1997;97:245–271.
80. Vergara JR, Estévez PA. A review of feature selection methods based on mutual information. *Neural Comput Appl* 2014;24:175–186.

81. Kalina J, Schlenker A. A Robust Supervised Variable Selection for Noisy High-Dimensional Data. *BioMed Res Int* 2015;2015:.
82. Yu L, Liu H. Efficient Feature Selection via Analysis of Relevance and Redundancy. *J Mach Learn Res* 2004;5:1205–1224.
83. Friedman JH, Bentley JL, Finkel RA. An Algorithm for Finding Best Matches in Logarithmic Expected Time. *ACM Trans Math Softw* 1977;3:209–226.
84. Bloch F. Nuclear Induction. *Phys Rev* 1946;70:460–474.
85. Purcell EM, Torrey HC, Pound RV. Resonance Absorption by Nuclear Magnetic Moments in a Solid. *Phys Rev* 1946;69:37–38.
86. Hawkes RC, Holland GN, Moore WS, Worthington BS. Nuclear Magnetic Resonance (NMR) Tomography of the Brain: A Preliminary Clinical Assessment with Demonstration of Pathology. *J Comput Assist Tomogr* 1980;4:577–586.
87. Smith FW, Hutchison JM, Mallard JR, Johnson G, Redpath TW, Selbie RD, Reid A, Smith CC. Oesophageal carcinoma demonstrated by whole-body nuclear magnetic resonance imaging. *Br Med J Clin Res Ed* 1981;282:510–512.
88. Morris PG. *Nuclear magnetic resonance imaging in medicine and biology*. Clarendon Press; 1986.
89. Levitt MH, Southampton U of. *Spin Dynamics: Basics of Nuclear Magnetic Resonance*. John Wiley & Sons; 2001.
90. Brown RW, Cheng Y-CN, Haacke EM, Thompson MR, Venkatesan R. *Magnetic Resonance Imaging: Physical Principles and Sequence Design*. John Wiley & Sons; 2014.
91. Hanson LG. Is quantum mechanics necessary for understanding magnetic resonance? *Concepts Magn Reson Part A* 2008;32A:329–340.
92. Hendrick RE, editor. Tissue Relaxation. *Breast MRI Fundam Tech Asp* New York, NY: Springer; 2008. p. 19–29.doi:10.1007/978-0-387-73507-8_2.

93. Bankier AA, O'Donnell CR, Mai VM, Storey P, Maertelaer VD, Edelman RR, Chen Q. Impact of lung volume on MR signal intensity changes of the lung parenchyma. *J Magn Reson Imaging* 2004;20:961–966.
94. Mulkern R, Haker S, Mamata H, Lee E, Mitsouras D, Oshio K, Balasubramanian M, Hatabu H. Lung Parenchymal Signal Intensity in MRI: A Technical Review with Educational Aspirations Regarding Reversible Versus Irreversible Transverse Relaxation Effects in Common Pulse Sequences. *Concepts Magn Reson Part Bridg Educ Res* 2014;43A:29–53.
95. Bergin CJ, Noll DC, Pauly JM, Glover GH, Macovski A. MR imaging of lung parenchyma: a solution to susceptibility. *Radiology* 1992;doi:10.1148/radiology.183.3.1584917.
96. Wild JM, Marshall H, Bock M, Schad LR, Jakob PM, Puderbach M, Molinari F, Van Beek EJ, Biederer J. MRI of the lung (1/3): methods. *Insights Imaging* 2012;3:345–353.
97. Parizel PM, Riet BV, van Hasselt BAAM, Van Goethem JW, van den Hauwe L, Dijkstra HAJ, van Wiechen PJ, De Schepper AM. Influence of Magnetic Field Strength on T2* Decay and Phase Effects in Gradient Echo MRI of Vertebral Bone Marrow. *J Comput Assist Tomogr* 1995;19:465.
98. Carr HY. Steady-State Free Precession in Nuclear Magnetic Resonance. *Phys Rev* 1958;112:1693–1701.
99. Bieri O, Scheffler K. Fundamentals of balanced steady state free precession MRI: Fundamentals of Balanced SSFP MRI. *J Magn Reson Imaging* 2013;38:2–11.
100. Scheffler K, Lehnhardt S. Principles and applications of balanced SSFP techniques. *Eur Radiol* 2003;13:2409–2418.
101. Herborn CU, Watkins DM, Runge VM, Gendron JM, Montgomery ML, Naul LG. Renal arteries: comparison of steady-state free precession MR angiography and contrast-enhanced MR angiography. *Radiology* 2006;239:263–268.
102. Stuber M, Weiss RG. Coronary magnetic resonance angiography. *J Magn Reson Imaging JMRI* 2007;26:219–234.

103. Mai VM, Chen Q, Li W, Hatabu H, Edelman RR. Effect of respiratory phases on MR lung signal intensity and lung conspicuity using segmented multiple inversion recovery turbo spin echo (MIR-TSE). *Magn Reson Med* 2000;43:760–763.
104. Chéfd'hotel C, Hermosillo G, Faugeras O. Flows of diffeomorphisms for multimodal image registration. *Proc IEEE Int Symp Biomed Imaging* 2002. p. 753–756.doi:10.1109/ISBI.2002.1029367.
105. Chéfd'Hotel C, Hermosillo G, Faugeras O. A variational approach to multi-modal image matching. *Proc IEEE Workshop Var Level Set Methods Comput Vis* 2001. p. 21–28.doi:10.1109/VLSM.2001.938877.
106. Shannon CE. Communication in the Presence of Noise. *Proc IRE* 1949;37:10–21.
107. Kjørstad Å, Corteville DMR, Henzler T, Schmid-Bindert G, Zöllner FG, Schad LR. Non-invasive quantitative pulmonary V/Q imaging using Fourier decomposition MRI at 1.5T. *Z Für Med Phys* 2015;25:326–332.
108. Veldhoen S, Weng AM, Wirth C, Kunz AS, Knapp JN, Stäb D, Segerer F, Hebestreit HU, Bley TA, Köstler H. Pulmonary Phase Imaging using Self-Gated Fourier Decomposition MRI in Patients with Cystic Fibrosis. *Proc 24th Annu Meet ISMRM* Singapore: 2016. p. 114.
109. Bauman G, Eichinger M, Uecker M. High temporal resolution radial bSSFP sequence with nonlinear inverse reconstruction for the measurement of the pulmonary blood inflow time using Fourier decomposition MRI. *Proc 20th Annu Meet ISMRM* Melbourne, Australia: 2012. p. 1340.
110. Bauman G, Puderbach M, Deimling M, Jellus V, Chéfd'hotel C, Dinkel J, Hintze C, Kauczor H-U, Schad LR. Non-contrast-enhanced perfusion and ventilation assessment of the human lung by means of fourier decomposition in proton MRI. *Magn Reson Med* 2009;62:656–664.
111. Fischer A, Weick S, Ritter CO, Beer M, Wirth C, Hebestreit H, Jakob PM, Hahn D, Bley T, Köstler H. Self-gated Non-Contrast-Enhanced FUnctional Lung imaging (SENCEFUL) using a quasi-random fast low-angle shot (FLASH) sequence and proton MRI. *NMR Biomed* 2014;27:907–917.

112. Bagchi S, Mitra SK. The Nonuniform Discrete Fourier Transform. In: Marvasti F, editor. *Nonuniform Sampl Theory Pract* Boston, MA: Springer US; 2001. p. 325–360.doi:10.1007/978-1-4615-1229-5_7.
113. Harris FJ. On the use of windows for harmonic analysis with the discrete Fourier transform. *Proc IEEE* 1978;66:51–83.
114. Meyer Y, Salinger DH. *Wavelets and Operators*. Cambridge University Press; 1993. doi:10.1017/CBO9780511623820.
115. Boashash B. Estimating and interpreting the instantaneous frequency of a signal. I. Fundamentals. *Proc IEEE* 1992;80:520–538.
116. Thakur G, Wu H-T. Synchrosqueezing-Based Recovery of Instantaneous Frequency from Nonuniform Samples. *SIAM J Math Anal* 2011;43:2078–2095.
117. Daubechies I, Lu J, Wu H-T. Synchrosqueezed wavelet transforms: An empirical mode decomposition-like tool. *Appl Comput Harmon Anal* 2011;30:243–261.
118. Thakur G, Brevdo E, Fučkar NS, Wu H-T. The Synchrosqueezing algorithm for time-varying spectral analysis: Robustness properties and new paleoclimate applications. *Signal Process* 2013;93:1079–1094.

7. Acknowledgements

I would like to gratefully acknowledge the guidance, support and encouragement of my doctoral advisor, Prof. Dr. med. Julien Dinkel, and thank him for the opportunity to use and expand my knowledge in medical imaging technologies.

I would like to thank Prof. Dr. med. Jens Ricke and the former director Prof. Dr. med. Maximilian Reiser for the opportunity to do a doctorate at LMU Munich.

My gratitude extends to Prof. Dr. med. Frank Reichenberger and Dr. med. Edith Silbernagel for their enthusiasm and willingness to provide both data and clinical expertise in the topic of probe based confocal endomicroscopy.

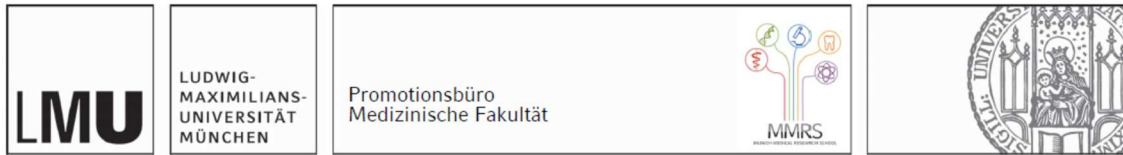
Special thanks go to Dr. rer. nat. Moritz Schneider, who co-advised me with through technical questions with astounding competence and professional wisdom. Further thanks go to Prof. Dr. rer. nat. Olaf Dietrich who contributed to my research with his rich scientific competence, professional support and willingness to delve into deep discussions.

I am incredibly happy to have worked with such supportive colleagues (Thomas, Lukas, Andreas, Konstantin, Astrid, Carolin, Balthasar, Phillip, ...), who were always willing to lend an ear.

I would also like to thank Prof. Dr. rer. nat. Michael Ingrisich and Dr. rer. biol. hum. Michael Peller for valuable discussions that many times opened up a new perspective for me.

Lastly, I would like to thank Deutsches Zentrum für Lungenforschung (DZL), whose funding facilitated my introduction to the vast international scientific community.

8. Affidavit



Eidesstattliche Versicherung

Bondesson, David

Name, Vorname

Ich erkläre hiermit an Eides statt, dass ich die vorliegende Dissertation mit dem Titel:

Novel image processing methods for characterizing lung structure and function

selbständig verfasst, mich außer der angegebenen keiner weiteren Hilfsmittel bedient und alle Erkenntnisse, die aus dem Schrifttum ganz oder annähernd übernommen sind, als solche kenntlich gemacht und nach ihrer Herkunft unter Bezeichnung der Fundstelle einzeln nachgewiesen habe.

Ich erkläre des Weiteren, dass die hier vorgelegte Dissertation nicht in gleicher oder in ähnlicher Form bei einer anderen Stelle zur Erlangung eines akademischen Grades eingereicht wurde.

Hamburg, 07.01.2021

Ort, Datum

David Bondesson

Unterschrift Doktorandin bzw. Doktorand